AFCRL-71-0358

THE MEASUREMENT OF SPATIAL AND TEMPORAL DISTRIBUTION OF RADIATION, USING A TALBOT SPECTROMETER

by

Adolf W. Lohmann
Donald E. Silva
Department of Applied Physics and Information Science
University of California, San Diego
La Jolla, California 92037

SECOND ANNUAL REPORT
30 June 1971

Contract Monitor: Thomas P. Condron
Optical Physics Laboratory

Approved for public release; distribution unlimited

Advanced Research Projects Agency
ARPA Order No. 1366

Monitored by
AIR FORCE CAMBRIDGE RESEARCH LABORATORIES
AIR FORCE SYSTEMS COMMAND
UNITED STATES AIR FORCE
BEDFORD, MASSACHUSETTS 01730

52

Unclassified

Security Classification

DOCUMENT CONTROL DATA - R & D

(Security classification of title, body of abstract and indexing annotation must be entered when the overall report is classified)

1. ORIGINATING ACTIVITY (Corporate author)

University of California, San Diego
Dept.of Applied Physics & Information Science
La Jolla, California 92037

2a. REPORT SECURITY CLASSIFICATION

Unclassified

2b. GROUP

3. REPORT TITLE

THE MEASUREMENT OF SPATIAL AND TEMPORAL DISTRIBUTION OF RADIATION, USING A TALBOT SPECTROMETER

4. DESCRIPTIVE NOTES (Type of report and inclusive dates)

Scientific. Interim.

5. AUTHOR(S) (First name, middle initial, last name)

Adolf W. Lohmann
Donald E. Silva

6. REPORT DATE

June 30, 1971

7a. TOTAL NO. OF PAGES

51

7b. NO. OF REFS

8

8a. CONTRACT OR GRANT NO.

F 19628-69-C-0268 ARPA Order No.

b. PROJECT, Task, Work Unit Nos. 1366 8692 n/a n/a

c. DOD ELEMENT 62301D

d. DOD SUBELEMENT n/a

9a. ORIGINATOR'S REPORT NUMBER(S)

Second Annual Report

9b. OTHER REPORT NO(S) (Any other numbers that may be assigned this report)

AFCRL-71-0358

10. DISTRIBUTION STATEMENT

A - Approved for public release; distribution unlimited.

11. SUPPLEMENTARY NOTES

This research was supported by the Advanced Research Projects Agency

12. SPONSORING MILITARY ACTIVITY

Air Force Cambridge Research Laboratories (OP)
L.G. Hanscom Field
Bedford, Massachusetts 01730

13. ABSTRACT

A Simulation Game to train data processors in optimal data recovery techniques is included in this report. Also, we studied the triple-multiplexing response to a point source for a future scanning spectrometer. Three basic motions are required to modulate the wavelength and angular coordinates of the source. When performing preliminary experiments with the Multiplex Scanner, we discovered that the underlying Talbot effect is useful also for measuring phase objects. The theory of this new "Talbot Interferometer" is explored and experimental results of a candle flame are reported. For axially symmetric objects, this setup is modified by replacing the straight line gratings with circular gratings. In this way the radial gradient of the deformed wavefront is observed. Finally a means of simply, yet accurately collimating a light source using the Talbot Interferometer is described.

DD FORM 1 NOV 68 1473

Unclassified

Security Classification

14 KEY WORDS	LINK A		LINK B		LINK C	
	ROLE	WT	ROLE	WT	ROLE	WT
Infrared, spectrometer, interferometer, grating, diffraction, spatial filtering, signal processing.						

Program code no.....1E50

Effective date of contract.....29 May 1969

Contract expiration date.....29 May 1972

Principal investigator and phone no.....Prof. Adolf W. Lohmann/
714 453-2000 ext. 2747

Project Scientist or Engineering and phone no....Thomas P. Condron/617 861-4852

Qualified requestors may obtain additional copies from the Defense Documentation Center. All others should apply to the National Technical Information Service.

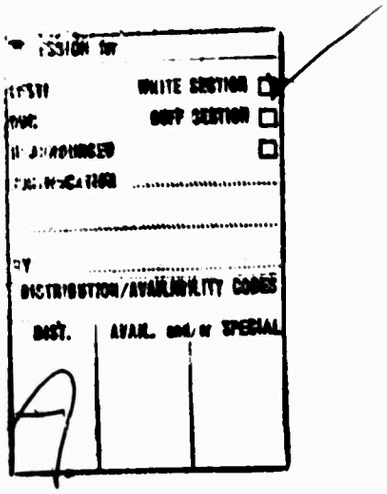

AFCRL-71-0358

THE MEASUREMENT OF SPATIAL AND TEMPORAL DISTRIBUTION OF RADIATION, USING A TALBOT SPECTROMETER

by

Adolf W. Lohmann
Donald E. Silva
Department of Applied Physics and Information Science
University of California, San Diego
La Jolla, California 92037

SECOND ANNUAL REPORT
30 June 1971

Contract Monitor: Thomas P. Condron
Optical Physics Laboratory

Approved for public release; distribution unlimited

Advanced Research Projects Agency
ARPA Order No. 1366

Monitored by
AIR FORCE CAMBRIDGE RESEARCH LABORATORIES
AIR FORCE SYSTEMS COMMAND
UNITED STATES AIR FORCE
BEDFORD, MASSACHUSETTS 01730

Abstract

A Simulation Game to train data processors in optimal data recovery techniques is included in this report. Also, we studied the triple-multiplexing response to a point source for a future scanning spectrometer. Three basic motions are required to modulate the wavelength and angular coordinates of the source. When performing preliminary experiments with the Multiplex Scanner, we discovered that the underlying Talbot effect is useful also for measuring phase objects. The theory of this new "Talbot Interferometer" is explored and experimental results of a candle flame are reported. For axially symmetric objects, this setup is modified by replacing the straight line gratings with circular gratings. In this way the radial gradient of the deformed wavefront is observed. Finally a means of simply, yet accurately collimating a light source using the Talbot Interferometer is described.

Table of Contents

Introduction

The goal is to measure infrared radiation from a balloon at an elevation of 30 km. Maximum coverage of the sky by the scanning spectrometer during the flight of the balloon is desired. To this end our previous Annual Report of 30 June 1970 devoted its efforts in describing: (1) the optimum scanning mode for the existing LMSC instrument, (2) a scheme for processing the data gathered by this instrument and (3) a future instrument based on the Talbot effect. Our efforts since then have been to support data processing for the existing equipment (see §2) and to continue the exploration of future methods of instrumentation (§1).

During our investigation of the scanning spectrometer we found that the collimating lens had to be good. Furthermore, it was discovered that the Talbot interferometer could be set up to test the lens and other optical components (§3 and Appendix A). The straight line gratings of our setup laterally shears the wavefront that passes through the test object, giving multiple-interferences. Our theory showed that if we allow only the zeroth diffracted order to pass to the plane of observation, the second derivative of the object transmittance would be observed. On the other hand if either of the first diffracted orders were allowed to pass, then we would observe the first derivative. Good collimation of the light source was a critical factor in this experiment. By separating the two gratings to a maximum distance over which interference could still be observed, a very sensitive test of the degree of collimation was obtained (§4 and Appendix B). Objects with axial symmetry are best tested by interferometers that radially shear the deformed wavefront. For this reason we modified our Talbot interferometer by replacing the straight line gratings with circular gratings. Our theory and experiments are not quite complete. We report here on the theory of the Talbot effect in cylindrical coordinates for axially symmetric objects (§5).

§1 The Scanning Spectrometer

In the previous Annual Report of 30 June 1970, a spectrometer based on the Talbot effect was described. A schematic representation of this instrument is shown in Figure 1. Sources to be observed are assumed to be sufficiently far away so that waves impinging upon the first grating are essentially plane. We use the collimating lens and point source to simulate a sky scene. The plane wave is diffracted by the first grating and the Talbot images so formed are detected by the second grating. The photodiode receiver collects the light which passes through both gratings. There are three variables of interest in the spectrum of a source, namely the wavelength and the elevation and azimuth angles that locate the direction from which the radiation is emitted. Since we have essentially only one signal parameter (i.e. the intensity of light source on the photodiode current), a triple-multiplexing scheme is required in order to place the three parameter function onto the one-parameter signal. The following motions of the spectrometer will accomplish this task. The movement of the second grating in the x-direction is used for obtaining cosinusoidal coding of the frequency of the spectrum. Rotation of the instrument will encode the angular position of the sources (α, β) and z-motion of the second grating

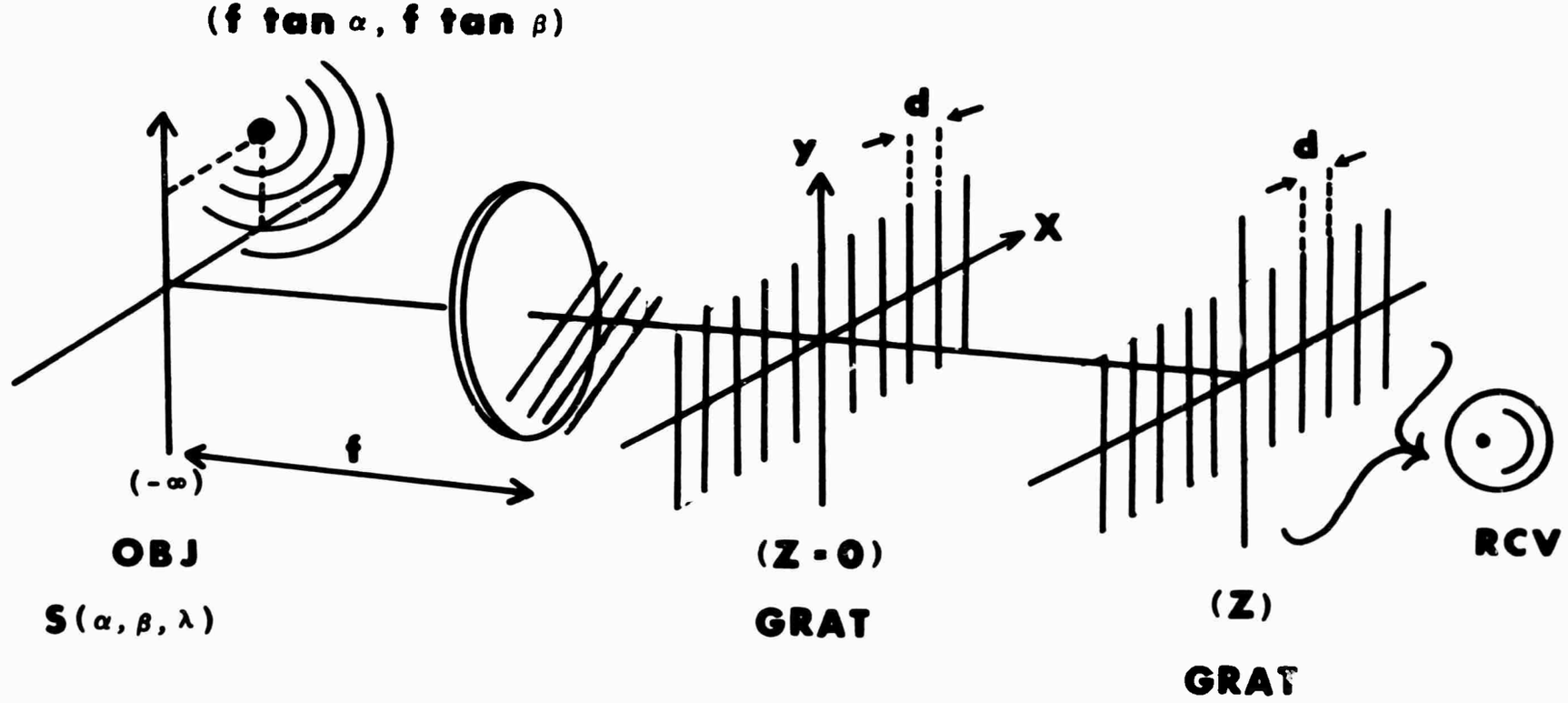

Figure 1
Basic Setup of the Multiplex Scanner

will increase the delay time for good spectral resolution and is necessary to recover the spectrum.

Our studies of the triple-multiplexing response to a point source for this instrument show that we have three main carrier frequencies produced as a consequence of the three independent motions. They are: $\omega_{lat} = 2\pi v_x/d$; $\omega_{long} = \pi v_z \lambda/d^2$; and $\omega_{ang} = \dot{\varphi}$. Here v_x and v_z are the velocities in the x- and z-directions, d is the grating period, λ is the wavelength of the radiation, $\dot{\varphi}$ is the time derivative of the angular position φ of the point source as shown in Fig. 1, and ω_{lat}, ω_{long}, ω_{ang} are the carrier frequencies associated with the x- and z-direction and the rotational motions respectively. The relative motions will have to be regulated in a manner so that the three main carrier frequencies can be separated. This in turn will be determined by the desired resolutions of the three spectrum parameters (λ, α, β). The analysis is incomplete but a detailed report will be made later.

§2 A Simulation Game

A "Signal Processing Game" was devised for the purpose of training the person in charge of signal processing whom we call the "investigator". The game consists of digital data (64 samples) which describe a signal plus noise. The investigator is supposed to devise a strategy for improving the signal-to-noise ratio. In problem #1 the investigator knows very little about the statistical behavior of signal and noise. Hence only a mild improvement is possible. In the subsequent problems the investigator is supplied with more and more statistical information, which allow for better and more sophisticated data improvement schemes.

The rules request that the game keeper hand the "Introduction" and "Recorded Data" sections to the investigator. Next the game keeper gives the investigator problem #1. It is important that only one problem be given the investigator at a time, because the formulation of problem #2 reveals part of the answer to #1. Also the last section, "About the Signal Synthesis", should be well-hidden from the investigator since it explains everything which the "investigator" shall find for himself, among others the correct noise-free signal.

§2.1 Introduction to a Signal Processing Game

The aim of this game is to develop skills in signal processing. At the same time errors in the computer program for this job will become apparent.

The definitions are essentially those of the 1970 final report. Notice: there is an error on pg. 38 of that report. In the denominator of equ. (13.18) $|\tilde{n}_E|^2$ should read $|\tilde{n}_E/\tilde{E}|^2$.

The input data for this game are the recorded data $U_R(t)$. It is assumed that the non-uniform scanning velocity of the spinning gondola has been corrected for already. The time coordinate is given in discreet numbers t = 0, 1, 2...63. We may consider $U_R(t)$ as being about one quarter of a single horizontal scan (β = constant).

The rules of the games are as follows. The "investigator" gets the sheet "Recorded Data $U_R(t)$" and the sheet "Problem #1". After solving this problem he will give the solution to the "monitor" and to the "game constructor". Now he may start on problem #2, and so on. But it is *important* that the investigator does not get the next problem sheet before he has finished the previous problem. The reason is that the formulation of the later problems contains parts of the answers to the earlier problems. This has to do with the basic structure of this simulation game: for performing any meaningful signal processing operation one must have some knowledge about the original signal and/or the noise. For example in problem #1 the investigator is told that the noise is additive and non-negative. In the later problems the investigator will be supplied with even more *a priori* information. Naturally, this should enable him to extract the signals better and better. But the methods for doing this

increase in complexity.

On the very last pages, following the problems, the design of the "recorded data" is explained, and the true original signal is unveiled. Obviously those pages should not be given to the investigator before he has solved all the problems.

§2.2 Recorded Data $U_R(t)$

t is the discrete time variable, running from t=0 to t=63.

t	$U_R(t)$	t	$U_R(t)$	t	$U_R(t)$	t	$U_R(t)$
0	55	16	110	32	39	48	383
1	25	17	184	33	56	49	10
2	85	18	29	34	05	50	69
3	61	19	51	35	15	51	58
4	20	20	42	36	95	52	52
5	95	21	78	37	09	53	66
6	07	22	09	38	81	54	79
7	00	23	15	39	21	55	134
8	62	24	13	40	81	56	94
9	79	25	50	41	399	57	102
10	148	26	99	42	372	58	108
11	105	27	54	43	348	59	94
12	125	28	99	44	303	60	56
13	125	29	35	45	383	61	67
14	173	30	98	46	317	62	51
15	181	31	02	47	317	63	63

§2.3 Problems

Problem #1

Given are the recorded data $U_R(t)$ with $t = 0, 1...63$. Wanted are the original data $U_0(t)$, which represent the "one-dimensional equivalent object radiation" $S_E(\alpha)$. We assume that the known influences of the telescope [M(x',y'); R(x',y')] and of the electrical system [G(t)] have been compensated already or are negligible. But the recorded signal $U_R(t)$ is corrupted by additive noise N(t):

$$U_R(t) = U_0(t) + N(t).$$

The only features known about the original signal $U_0(t)$ and about the noise N(t) are that they are non-negative:

$$U_0(t) \geq 0; \qquad N(t) \geq 0.$$

Furthermore the noise N(t) is stationary, which means that the noise properties are not "drifting". In other words, short-term average features of the noise remain the same from the beginning to the end of the observation.

Try to utilize the given *a priori* information for computing a new signal $U_1(t)$ from $U_R(t)$, which somehow is better than $U_R(t)$ as an approximated representation of $U_0(t)$. Plot $U_1(t)$ as a continuous curve, and also $U_R(t)$ for comparison.

Problem #2

Given are the facts:

$$U_0(t) \geq 0; \qquad N(t) \geq 0; \qquad \bar{N} = 50.$$

By $\bar{N}$ we mean the linear average of the noise. This $\bar{N}$ can be visualized as the dark current of the photoreceiver as measured with an instrument which rejects high frequencies.

Based on these facts try to compute a better signal $U_2(t)$ from $U_R(t)$. Plot both $U_2(t)$ and $U_R(t)$.

(to be cut by game monitor)

Problem #3

Given are the same facts as in the previous problem. In addition it is known that the noise is approximately "white".

$$N(t) = \bar{N} + n(t); \qquad \tilde{n}(\nu) = \int n(t)\, e^{-2\pi i \nu t}\, d\nu;$$

$$\nu = m/64; \quad m = -32, -31, \ldots -1, 0, +1, \ldots +30, +31;$$

$|\tilde{n}(\nu)|^2 \approx$ constant. The value of this "constant" is not known. Try to deduce it from the recorded data $U_R(t)$. You might have to make an intelligent guess.

Problem #4

Given are the same facts as in the previous problem, including the "constant" which describes the noise power level.

$$|\tilde{n}(\nu)|^2 \approx \frac{16}{3}\,10^4 \text{ in } -\frac{1}{2} \leq \nu \leq +\frac{1}{2}.$$

Now that $|\tilde{n}(\nu)|^2$ is known and $U_R(t)$ is computable, can you apply the Wiener-filter theory, at least in a guessed approximation? Try it and compute $U_4(t)$. Plot $U_4(t)$ and $U_R(t)$. Hint: represent $|\tilde{U}_0(\nu)|^2$ by a gaussian function of suitable peak power and width. Signal processing specialists always try it with a gaussian function if they don't know a better way.

$$|\tilde{U}_0(\nu)|^2 \approx P_4\, e^{-\pi(\nu/\nu_4)^2}.$$

(to be cut by game monitor)

Problem #5

Try the same approach as in the previous problem, but with a guessed sinc^2-shaped $|U_0(\nu)|^2$.

$$|U_0(\nu)|^2 \approx P_5\, \text{sinc}^2(\nu/\nu_5); \qquad \text{sinc } z = \frac{\sin \pi z}{\pi z}$$

Plot the result $U_5(t)$ and also $U_R(t)$ for comparison.

Problem #6

Try the same approach as in the previous problem, but a somewhat different guess for $|\tilde{U}_0(\nu)|^2$:

$$|\tilde{U}_0(\nu)|^2 = P_6 \, \mathrm{sinc}^2(\nu/\nu_6) + (P_0 - P_6)\delta_0;$$

Herein δ_0 means a function which is equal to 1 for $\nu = 0$ and equal to 0 for $\nu \neq 0$. Plot $U_6(t)$ and $U_R(t)$.

(to be cut by game monitor)

Problem #7

Based on all of the accumulated experience try your own signal processing approach or simply guess what $U_0(t)$ might have been. Call it $U_7(t)$. Plot $U_7(t)$ and $U_R(t)$.

§2.4 About the Signal Synthesis

The noise N(t) covers a time range t = 0, 1, 2...63 and an amplitude range $0 \leq N(t) \leq 99 = N$. The values for N(t) are picked from a table of random numbers. Hence we may assume

$$\overline{N(t)} = N/2 \approx 50; \qquad N = 99;$$

$$N(t) = \bar{N} + n(t); \qquad -N/2 \leq N(t) \leq +N/2.$$

Since the time resolution step is $\delta t = 1$ the frequency range $\Delta\nu$ is $\Delta\nu = 1/\delta t = 1$:

$$-\frac{1}{2} \leq \nu \leq +\frac{1}{2}\ .$$

The time duration Δt is $\Delta t = 64$. Hence the frequency resolution is $\delta\nu = 1/\Delta t = 1/64$. In other words the Fourier transformation by means of a digital computer provides a frequency spectrum at $\nu = -32/64, -31/64, \ldots -1/64, 0, +1/64, \ldots +31/64$.

Since n(t) has a zero-mean, and since n(t) consists of (almost) unrestrained random numbers, we may expect a "white" noise power spectrum.

$$\langle |\mathfrak{n}(\nu)|^2 \rangle = \text{constant} \cdot \text{rect}(\nu);$$

$$\text{rect}(\nu) = \begin{cases} 1 \text{ in } -\frac{1}{2} \leq \nu \leq +\frac{1}{2} \\ 0 \text{ elsewhere} \end{cases}$$

The value of the constant can be computed on the basis of the Plancherel-theorem:

$$\int |\mathfrak{n}(\nu)|^2 \, d\nu = \int |n(t)|^2 \, dt.$$

The right-hand side will be computed based on the histogram-method. It is obviously:

$$\int_0^T |n(t)|^2 \, dt = T \, \overline{|n(t)|^2}$$

The probability for n is constant between -N/2 and +N/2, the constant being defined by the normalization integral

$$p(n) = \text{constant} \cdot \text{rect}(n/N);$$

$$1 = \int p(n)\, dn = N \cdot \text{constant}; \quad \text{constant} = 1/N.$$

Now we can compute the mean square of n(t) by means of the histogram method:

$$\overline{|n(t)|^2} = \int n^2\, p(n)\, dn = (1/N) \int_{-N/2}^{+N/2} n^2\, dn = N^2/12.$$

Since it is

$$\int_{-\frac{1}{2}}^{+\frac{1}{2}} |\tilde{n}(\nu)|^2\, d\nu = \overline{|\tilde{n}|^2}$$

and

$$\int |n(t)|^2\, dt = T\, \overline{|n|^2} = T\, N^2/12$$

we conclude on the basis of the Plancherel theorem

$$\overline{|\tilde{n}|^2} = T\, N^2/12; \qquad \overline{|\tilde{n}|^2} = (16/3)\, 10^4.$$

In our case it is T = 64 and N ≈ 100.

Now we will devise the object. It shall consist of several square boxes, all with the same width B, but with different amplitudes A_m, and with center locations t_m:

$$U_0(t) = \sum_{m=1}^{M} A_m\, \text{rect}[(t - t_m)/B].$$

The number M indicates the totel number of square-boxes. We chose so that less than half of the time-domain is covered by square-boxes. The reletive coverage is given by:

$$\text{"relative coverage"} = MB/T.$$

We will select the locations t_m such that there is no overlep among square-boxes. The object spectrum is:

$$\tilde{U}_0(\nu) = \int U_0(t)\, e^{-2\pi i \nu t}\, dt$$
$$= \sum A_m\, B\, \text{sinc}(\nu B)\, e^{-2\pi i \nu t_m}.$$

The peak power is:

$$|\tilde{U}_0(0)|^2 = (\sum A_m B)^2 = B^2 (\sum A_m)^2.$$

At other frequencies the object power spectrum is:

$$|\tilde{U}_0(\nu)|^2 = B^2 \operatorname{sinc}^2(\nu B) \left|\sum A_m e^{-2\pi i \nu t_m}\right|^2.$$

The modulus-square expression can be re-written in a form suitable for computing the expectation value:

$$\left|\sum A_m e^{-2\pi i \nu_m t}\right|^2 = \sum\sum A_m A_j e^{-2\pi i \nu (t_m - t_j)} =$$

$$= \sum A_m^2 + \sum_{(m \neq j)}\sum A_m A_j e^{-2\pi i \nu (t_m - t_j)}.$$

The $\sum\sum(m \neq j)$ will not be exactly zero, but can be expected to be zero in average over the ν-domain (except for $\nu = 0$). Hence we get as expected value

$$\langle |\tilde{U}_0(\nu)|^2 \rangle = B^2 \operatorname{sinc}^2(\nu B) \sum A_m^2.$$

We may also compute the total power spectrum, most easily on the basis of the Plancherel theorem:

$$\int |U_0(\nu)|^2 \, d\nu = \int U_0^2(t) \, dt = B \sum A_m^2.$$

Requirements

The relative coverage of the time domain by square-box signals shall be less than 50%:

$$MB/T < \frac{1}{2}.$$

The sinc-square function of the object power spectrum shall cover not more than half of the frequency range. Specifically we request that the second zero of sinc-square is halfway out to the bandlimit 1/2:

$$\nu B = 2; \qquad \nu = 1/4 \quad B = 8.$$

Let the ratio of object power spectrum to noise power spectrum be about 2 at the second side-maximum of the sinc-square function. The second side maximum occurs at the argument 5/2. The sinc-square function is there $\operatorname{sinc}^2(5/2) = (5\pi/2)^{-2} \approx 16/1000$. Hence we request:

$$|\tilde{U}_0(5/2B)|^2 \approx B^2(16/1000) \sum A_m^2 = 2 \overline{|\tilde{n}|^2}.$$

It was $\overline{|\tilde{n}|^2} = T N^2/2$; $T = 64$; $N = 100$; $B = 8$. Hence we get:

$$\sum A_m^2 \approx 10\, N^2 = 10^5.$$

The relative coverage requirement yields with $B = 8$ and $T = 64$ for the number M of square-box signals $M < 4$. We will take $M = 3$, which corresponds to a relative coverage of 3/8.

Now we select the object amplitudes A_1, A_2, A_3. Let us introduce for convenience the term "relative amplitudes" by dividing the amplitudes by the mean noise value N/2: $a_m = A_m/(N/2) = 2A_m/N$. This reduces the former amplitude requirement to:

$$\sum (N/2)^2\, a_m^2 \approx 10\, N^2;\ \sum a_m^2 \approx 40.$$

We select now

$$a_1 = 6,\ a_2 = 2,\ a_1 = 1.$$

It is to be expected that the square-box #1 exceeds the noise clearly, the square-box #2 is barely bigger than the noise, while the third square-box will be very difficult to detect, if at all. Maybe it is not quite as based since the root-mean-square noise $\sqrt{\overline{(N(t) - \bar{N})^2}} = \sqrt{\overline{|n(t)|^2}} = \sqrt{N^2/12}$ is less than the mean noise $\bar{N} = N/2$.

The square-box positions t_m were chosen as $t_1 = 44.5$; $t_2 = 13.5$; $t_3 = 55.5$. The true original signal $U_0(t)$ is plotted below.

§3 The Talbot Interferometer

Testing optical components with the Talbot interferometer setup resulted from the necessity of having a good collimating lens for our scanning Talbot Spectrometer. Thus we have a sensitive and inexpensive means for testing these components. The Ronchi rulings used with the setup give us the lateral derivative of the wavefront deformed by the test object. Thus the deviations from the expected surface shape can be observed. The following is a detailed report that explains this setup.

§3.1 Introduction to the Application of the Talbot Effect for Measuring Phase Objects.

A phase object changes the amplitude of a wave passing through it by a constant factor but alters the phase from point to point, which yields a transmittance function $t(x, y) = a\, e^{i\phi(x,y)}$. Examples of phase objects are transparent biological objects whose index of refraction is nearly equal to that of its surrounding medium, and objects made of a transparent medium such as lenses and prisms. The techniques now available to examine phase objects include Zernike's phase contrast microscopy, interferometric methods, Ronchi grating techniques, Schlieren methods and moiré fringes.

The "Talbot effect"[1] is also known as "Fourier-imaging" or "self-imaging". As Talbot observed in 1836, an image of a grating is formed at a distance $2d^2/\lambda$ (where d = grating period) behind the grating, which has been illuminated by a monochromatic plane wave. The space between the grating and its Talbot image is empty. In other words the Talbot effect is a method for forming images of a periodic object without any lenses or mirrors. When properly modified the Talbot effect affords a unique method for quantitatively observing phase objects, through the use of two Ronchi rulings, one of which is self-imaged onto the second. The complete theory requires scalar wave diffraction theory and is presented in §3.3.

An explanation using rays will acquaint the reader with the basic operation of the instrument. However, this is only a crude explanation since it does not take into account the wave nature of light which results in some possibly useful color effects. Therefore in the third section wavelength considerations will be added to show the limitations and uniqueness of the instrument.

§3.2 Qualitative Explanation

A Ronchi ruling is illuminated with collimated light as shown in Figure 2. The diffracted waves are modulated and form"Fresnel Images"[2]. At integer multiples of the distance $z_T \approx 2d^2/\lambda$, where d is the grating period, an image of the Ronchi ruling is formed. If a second grating is placed at one of these image planes in anti-position to the image, no light will be transmitted beyond the second grating. Hence a ray that passes through a slit of the first grating is blocked by the second grating as shown in Figure 2. A prism of wedge angle α is introduced at a distance z from the second grating and normal to the incident rays. The rays passing through the prism will be bent through an angle ε. Thus the intensity of the light as seen by the observer varies with the angle ε as sketched in Figure 3, with peak intensities given by

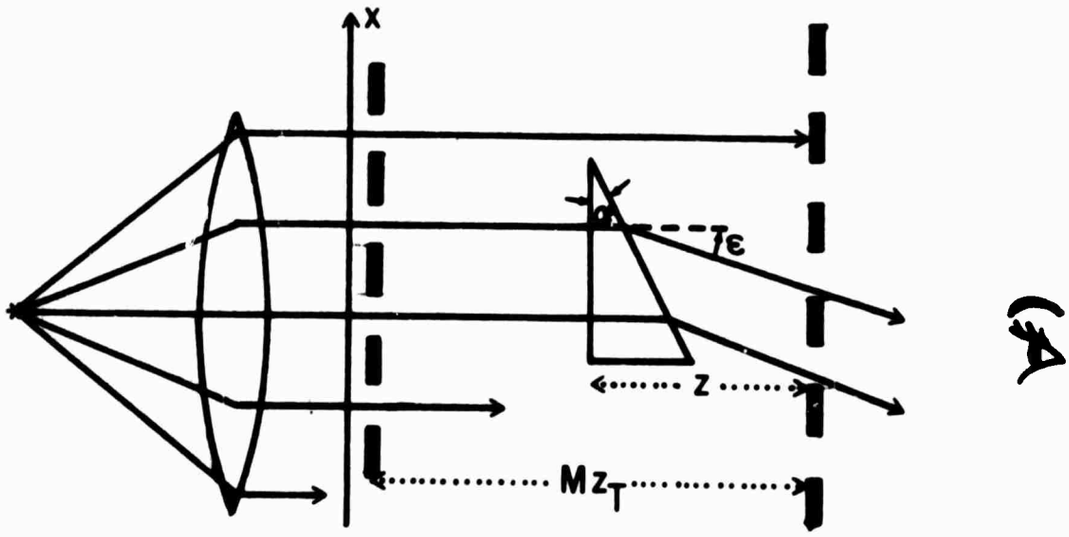

Figure 2. Basic instrument with a prism as a test object.

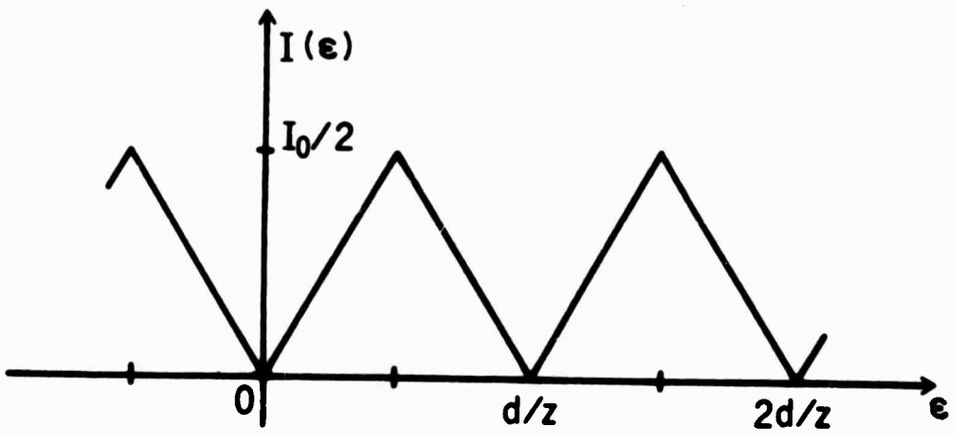

Figure 3. Inteneity as a function of the ray distribution.

$$\varepsilon \approx \tan \varepsilon_m \approx (m + 1/2)\, d/z$$

and dark fringes by

$$\varepsilon \approx \tan \varepsilon_m = md/z. \tag{1}$$

The angle ε is related to the wedge angle α under small angle approximation by

$$\varepsilon = (n - 1)\, \alpha. \tag{2}$$

A prism's thickness increases linearly with the distance from its apex, and the wedge angle α giving

$$\alpha \approx \tan \alpha = \Delta t/\Delta x, \quad \text{where } \Delta t = \text{prism thickness}, \quad \Delta x = \text{distance from apex.}$$

Now a phase object can be thought to be made up of prisms, a fact which is often used to explain the action of a lens, so that for any point (x, y) on the object, the prism angle α is given by

$$\alpha(x, y) \approx \frac{\partial t(x, y)}{\partial x}$$

which in turn is related to ε by substitution into (2)

$$\varepsilon(x, y) = (n - 1)\, \frac{\partial t(x, y)}{\partial x}\,. \tag{3}$$

The y derivative $\partial t(x, y)/\partial y$ is of no concern here since the grating bars are parallel to the y-axis.

Thus a dark fringe structure is obtained whenever $\varepsilon(x, y)$ meets the conditions of equation (1). Equations (1) and (3) are plotted in Figure 4 as a function of x. Dark fringes occur at the intersections of equations (1) and (3). In other words the fringes indicate lines of equal $\partial t/\partial x$, which is the x-component of the surface gradient Δt. Where the lines are close together, the slope $\partial t/\partial x$ changes rapidly. Hence the fringe density or fringe frequence is proportional to the x-component of the curvature $\partial^2 t/\partial x^2$. The maximum detectable curvature is determined by the minimum detectable fringe separation. In a sense what is observed is the second derivative of the phase object.

There are two problems of fringe detection. The first occurs when the fringes beoome too fine for the eye to resolve them. This is only a practical limitation and a magnifying glass would extend the sensitivity. But the second problem is more fundamental. The field of view is finite, say B = Nd, where N is the number of lines in the grating. For an object whose curvature is at the minimum detectable sensitivity its curvature must be large enough for at least one full (or maybe one-half) fringe across the field. Hence

$$\left[(\partial t/\partial x)_{max} - (\partial t/\partial x)_{min}\right] (n - 1) \geq d/2z.$$

If $(\partial t/\partial x)_{max}$ is at $x = + Nd/2$ and $(\partial t/\partial x)_{min}$ is at $x = -Nd/2$, then

$$\partial t(x + Nd/2, y)/\partial x \; - \; \partial t(x - Nd/2, y)/\partial x \approx \partial^2 t/\partial x^2\, Nd.$$

Hence,

$$\left|d^2 t/\partial x^2\right| \geq \frac{d/2}{z(n - 1)\, Nd} = \frac{1}{2Nz(n - 1)}\,. \tag{4}$$

The maximum Talbot distance is given by[3]

$$z_{max} = Nd^2/2\lambda.$$

Using this as z in equation (4) yields

$$|\partial^2 t/\partial x^2| \geq \frac{\lambda}{(Nd)^2(n-1)} = \frac{\lambda}{B^2(n-1)}$$

For example if $\lambda = 5 \times 10^{-4}$ mm, $n - 1 = 1/2$, $B = 10^2$ mm we obtain $|\partial^2 t/\partial x^2| \geq 10^{-7}$ mm^{-1} = 1/10 km.

As an example of the system a perfect thin lens is considered. The phase of this lens is given by[4]

$$\varphi(x, y) = (-\pi/\lambda f)(x^2 + y^2)$$

where f is the focal length of the lens, and (x, y) its coordinates. The relative phase of any object is

$$\varphi(x, y) = (2\pi/\lambda)(n - 1)\, t(x, y)$$

$$\therefore t(x, y) = -(x^2 + y^2)/[2f(n - 1)],$$

and

$$\partial t(x, y)/\partial x = -x/[(n - 1)f]$$

which when substituted into equation (3) gives

$$\varepsilon(x, y) = -x/f.$$

This is a straight line which when plotted onto Figure 4 gives equally-spaced fringes of fd/z. An imperfect lens will not have straight equally spaced fringes, whereby its quality can be determined.

It is worth noting that this system likewise tests the collimator objective and can serve as a good method for testing lenses. In addition the ability to completely darken the field behind the second grating is a test of the degree of collimation of the objective since converging or diverging waves produce moiré fringes behind the second grating due to unequal grating periods.

The work of Nishijima and Oster can be explained by rays.[5] However, on the other hand a complete explanation of our instrument requires the use of diffraction theory which accounts for the color effect and which explains the ultimate limitation of this instrument. The location of the grating image is wavelength dependent, a fact that has been exploited in designing filters and a spectrometer[6]. Furthermore, the complete setup (vide Figure 5) allows the selection of the first or second derivative of the phase object.

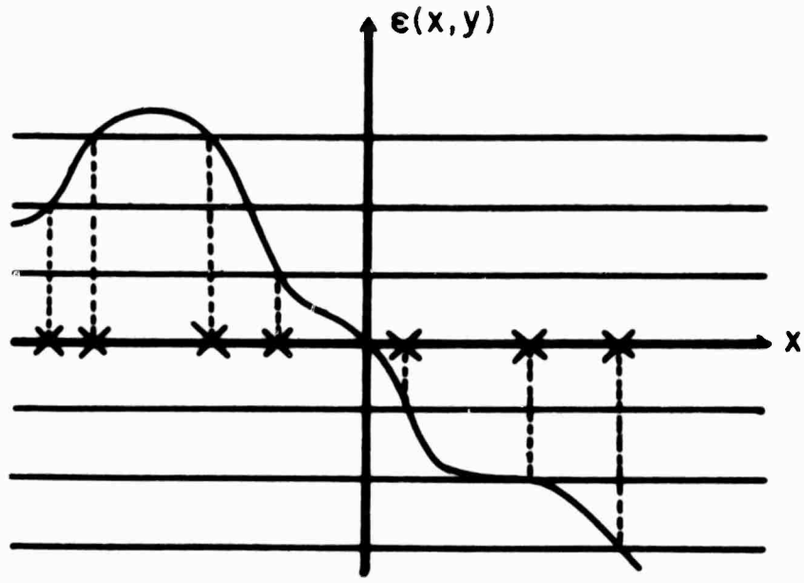

Figure 4. Plot of equations (1) and (3). Equation (1) is the set of horizontal straight lines. X marks the locations of the fringes for this test object.

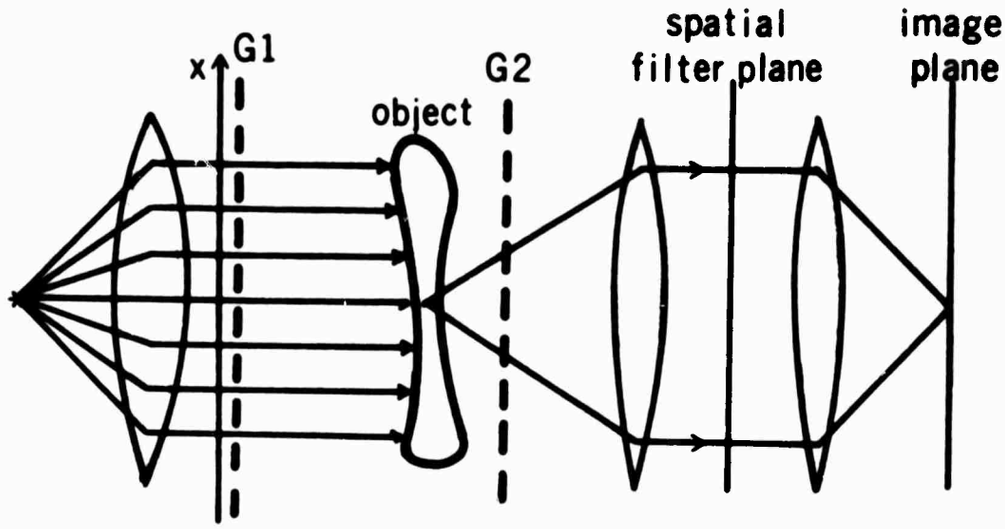

Figure 5. Test setup incorporating a spatial filter plane for selecting first or second derivative.

§3.3 Theoretical Explanation

The ray explanation, which is essentially due to Nishijima and Oster and is presented in §3.2, helped one to understand the basic operation of the instrument. In this section a rigorous derivation is presented based on scalar diffraction theory. The result will be an interpretation of the image as two, three or many shifted object wave fronts, sometimes tilted. Accordingly we will use the terms "shearing interferometry" as is common when two shifted object wavefronts interact. In generalization thereof we will introduce the terms "triple shearing interferometry" and "multiple shearing interferometry". In some instances these shearing interferences will represent the first or the second derivative of the object. The instrument is diagrammed in Figure 6, which illustrates the pertinent distances.

Consider a monochromatic plane wave incident on grating G1 in the plane at $-z_1$. The field behind this grating is

$$u(x, y, -z_1) = e^{-ikz_1} \sum_{n=-\infty}^{\infty} C_n e^{2\pi inx/d}$$

where the periodic grating is considered infinite in extent and of period d, and is expressed as a Fourier exponential series; $k = 2\pi/\lambda$ where λ = wavelength of light. Following a line of reasoning like Edgar's[7], the incident plane wave is by action of the grating replaced by a set of plane wavefronts whose x-direction cosines are $n\lambda/d$ and whose field strength is proportional to C_n. This gives a propagating field behind G1 as

$$u(x, y, z) = e^{-ikz_1} \sum_{n} C_n e^{ik[n\lambda x/d+(z_1+z)\sqrt{1-(n\lambda/d)^2}]}$$

which at the object plane z = 0 reduces to

$$u(x, y, 0-) = e^{-ikz_1} \sum_{n} C_n e^{ik[n\lambda x/d+z_1\sqrt{1-(n\lambda/d)^2}]}.$$

Applying the Kirchoff boundary conditions to the field as it passes through the object as we did through grating G1, we have

$$u(x, y, 0+) = e^{-ikz_1} \sum_{n} C_n u_0(x, y) e^{ik[n\lambda x/d+z_1\sqrt{1-(n\lambda/d)^2}]} \quad (5)$$

where $u_0(x, y)$ is the two dimensional object transmittance function.

Each of the plane waves is diffracted as it passes through the object. At this point, the concept of the angular spectrum is very useful.[8] In this formulation the diffraction phenomenon is a multiplicative quadratic phase factor $\exp(ikz\sqrt{1 - \lambda^2(\nu^2 + \mu^2)})$ in the Fourier domain which increases with the propagation distance z. Let $\tilde{u}(\nu, \mu; 0+)$ be the angular spectrum of equation (5) defined by

$$\tilde{u}(\nu, \mu; 0+) = \iint u(x, y, 0+) e^{-2\pi i(\nu x+\mu y)} dxdy$$

where the integration in this section will be over the interval $(-\infty, \infty)$ when unspecified, and (ν, μ) are the Fourier spatial frequency components. The

angular spectrum for the plane just preceding G2 ($z = z_2-$) is

$$\tilde{u}(\nu, \mu; z_2-) = \tilde{u}(\nu, \mu; 0+)\, e^{ikz_2\sqrt{1-\lambda^2(\nu^2+\mu^2)}}$$

$$= e^{-ikz_1} \sum_n C_n\, \tilde{u}_0(\nu - n/d, \mu)\, e^{ik[z_1\sqrt{1-(n\lambda/d)^2}+z_2\sqrt{1-\lambda^2(\nu^2+\mu^2)}]}$$

where $\tilde{u}_0(\nu, \mu)$ is the angular spectrum of the object. The Kirchoff boundary conditions are applied to the second grating at $z = z_2$.

$$u(x, y, z_2+) = u(x, y, z_2-) \sum_m C_m\, e^{i\pi m}\, e^{2\pi imx/d}$$

where the $e^{i\pi m}$ factor accounts for the fact that the second grating is shifted by half a period with respect to G1. In the Fourier domain this becomes a convolution which results in

$$\tilde{u}(\nu, \mu; z_2+) = e^{-ikz_1} \sum_n \sum_m C_n\, C_m\, e^{i\pi m}\, \tilde{u}_0(\nu - (n+m)/d, \mu)$$

$$e^{ik\{z_1\sqrt{1-(n\lambda/d)^2} + z_2\sqrt{1-\lambda^2[(\nu-m/d)^2+\mu^2]}\}} \qquad (6)$$

The image plane is conjugate to the object plane $z = 0$. Therefore we compute the field virtually back to the $z = 0$ plane in order to find the resultant field in the plane of observation, and give the field a new symbol $v(x, y)$ with $\tilde{v}(\nu, \mu)$ as its Fourier spectrum

$$\tilde{v}(\nu, \mu) = \tilde{u}(\nu, \mu; z_2+)\, e^{-ikz_2\sqrt{1-\lambda^2(\nu^2+\mu^2)}}.$$

Substituting equation (6) into this and simplifying by using the first two terms in the Taylor series expansion of the square roots in the exponential terms yields

$$\tilde{v}(\nu, \mu) = \sum_n \sum_m C_n\, C_m\, e^{i\pi m}\, \tilde{u}_0(\nu - (n+m)/d, \mu)\, e^{ik[z_2\lambda^2\nu m/d - z_1(n\lambda/d)^2 - z_2(m\lambda/d)^2]}.$$

But as explained in the first section the two gratings are separated by some multiple M of the Talbot distance z_T. Thus putting $z_2 + z_1 = M\, z_T \approx 2Md^2/\lambda$ into the above equation reduces it to

$$\tilde{v}(\nu, \mu) = \sum_n \sum_m C_n\, C_m\, e^{i\pi m}\, \tilde{u}_0(\nu - (n+m)/d, \mu)$$

$$e^{2\pi i[\lambda z_2 \nu m/d - z_2\lambda(m^2-n^2)/2d^2]}. \qquad (7)$$

Taking the Fourier transform of this gives the resultant field in the image plane.

$$v(x, y) = \sum_n \sum_m C_n\, C_m\, u_0(x + mz_2\lambda/d, y)\, e^{2\pi i[m/2+(m+n)^2 z_2/z_T+(n+m)x/d]} \qquad (8)$$

Thus multiple-shearing interferences are observed in the image plane. In ordinary shearing interference only two terms are present, $u(x + \Delta x, y) - u(x, y)$. In order to reduce the large number of terms of the double series we will perform certain spatial filtering operations. The field expressed by equation (7) is found in the spatial filter plane located one focal length behind the first lens of the telecentric system. In order to filter just the $n + m = 0$ or $n + m = 1$ term, which we will show leads to special interferences, we must

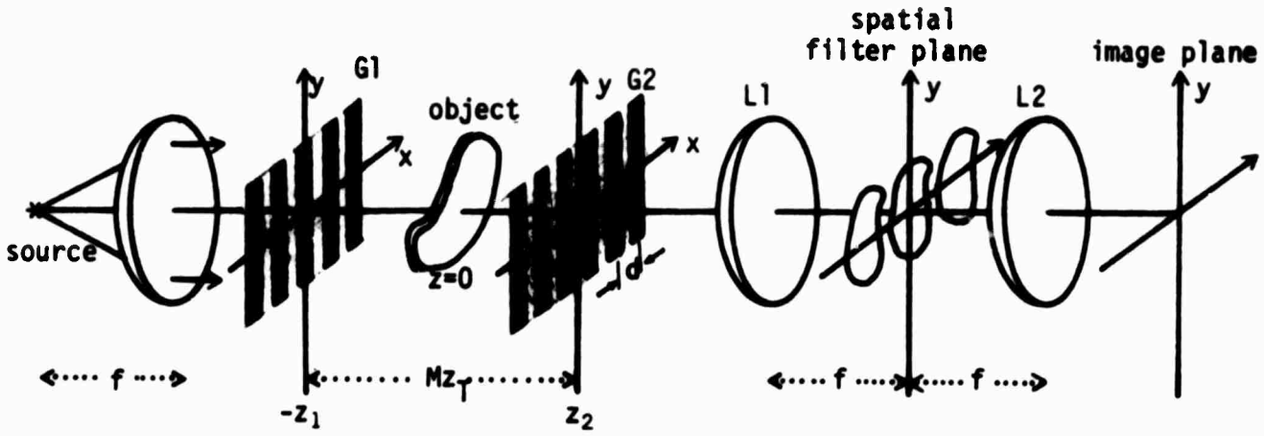

Figure 6. Talbot Interferometer setup. Telecentric system is focused onto the object. The spatial filter plane is used to simplify the multiple-shearing interferences.

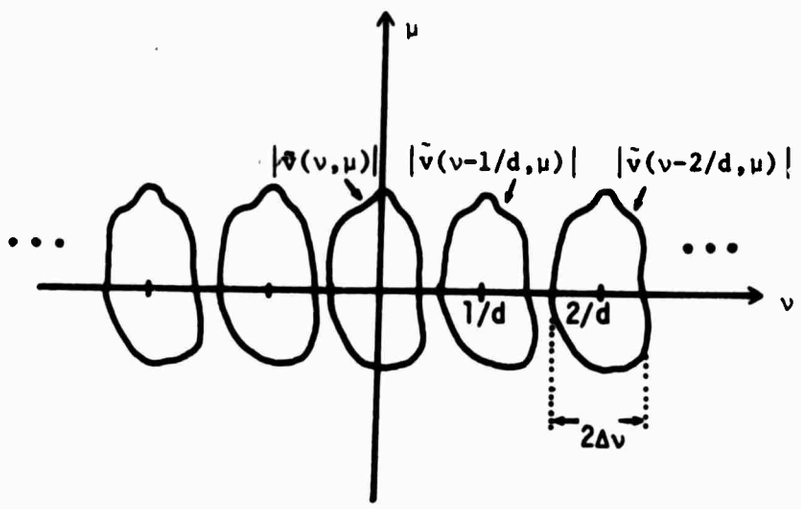

Figure 7. The spatial filter plane with an arbitrary object spectrum. The spectrum is shifted along the ν-axis by 1/d.

assume that the shifted spectrums $\hat{u}_0(\nu - (n+m)/d, \mu)$ do not overlap. This is shown in Figure 7 along with the bandwidth restriction of the object, $|\Delta\nu| \leq 1/2d$, i.e., $\hat{u}_0(\nu, \mu) = 0$ whenever $|\nu| \geq 1/2d$.

§3.4 Zero Order Filtering

The multiple shearing interferences can be simplified by spatial filtering. Our first consideration is the zero order filtering case, $n + m = 0$. Thus equation (8) reduces to

$$v(x, y) = \sum_m C_m C_{-m} e^{i\pi m} u_0(x + mz\lambda/d, y) \qquad (9)$$

where z_2 is written as z without the subscript 2 and is the distance from the object to the second grating. If we restrict ourselves to only considering either amplitude or phase modulated gratings that are symmetrical about the origin then C_m's are real and $C_m = C_{-m}$. Equation (9) becomes

$$v(x, y) = C_0^2\left\{u_0(x, y) + \sum_{m\neq 0} (C_m/C_0)^2 e^{i\pi m} u_0(x + mz\lambda/d, y)\right\}.$$

These multiple-shearing interferences can be simplified to triple-shearing interferences if $(C_m/C_0)^2$ terms for all but the first pair are negligibly small. By using a special grating whose transmittance is given by $g(x) = 1 + \cos(2\pi x/d)$, triple-shearing interferences would result, since $C_m = 0$, $|m| > 2$. Alternatively, a grating can be designed which is still binary and yet meet this condition.[9] We now consider the use of an inexpensive Ronchi ruling as the grating. The Fourier coefficients are $C_m = 1/2\ \mathrm{sinc}(m/2)$; all even $C_m = 0$, where $\mathrm{sinc}(x) = \sin(\pi x)/\pi x$. Thus

$$v(x, y) = C_0^2\left\{u_0(x, y) - \sum_{\substack{m\neq 0 \\ (\text{odd})}} \mathrm{sinc}^2(m/2)\, u_0(x + mz\lambda/d, y)\right\}. \qquad (10)$$

These multiple-shearing interferences can be approximated by triple-shearing interferences in this case since the $|m| = 3, 5, 7, \ldots$ terms can be neglected. The $|m| = 3$ term is only one-ninth that of the $|m| = 1$ term. Higher order terms are much smaller than this. Therefore equation (10) reduces approximately to

$$v(x, y) \approx 1/4\left\{u_0(x, y) - (2/\pi)^2 u_0(x + z\lambda/d, y) - (2/\pi)^2 u_0(x - z\lambda/d, y)\right\}. \qquad (11)$$

These triple-shearing interferences will sometimes be roughly the second derivative, $\partial^2 u/\partial x^2$ of the object if the shift $z\lambda/d$ is smaller than the resolution length δx, which is the inverse of the object bandwidth $\Delta\nu = 1/\delta x$. Actually $z\lambda/d = (1/3)\delta x$ is still good, as we will show by making use of the Bernstein theorem. First we expand the last two terms in equation (11) in a Taylor series around $z\lambda/d$.

$$u(x + z\lambda/d, y) = \sum_{p=0}^{\infty} u_0^{(p)}(x, y)\ 1/p!\ (z\lambda/d)^p$$

$$u_0(x - z\lambda/d, y) = \sum_{p=0}^{\infty} u_0^{(p)}(x, y)\ (-1)^p/p!\ (z\lambda/d)^p$$

where $u_0^{(p)}(x, y) = \partial^p u_0(x, y)/\partial x^p$. Therefore equation (11) becomes

$$v(x, y) = 1/4\Big\{u_0(x, y) - (2/\pi)^2 \left[2u_0(x, y) - 2 \sum_{p=2}^{\infty} u_0^{(p)}(x, y)\right.$$

$$\left. 1/p!\ (z\lambda/d)^p\right]\Big\}.$$

The summation term can be approximated by the second derivative, i.e.,

$$\sum_{\substack{p=2 \\ (\text{even})}}^{\infty} u_0^{(p)}(x, y)\ 1/p!\ (z\lambda/d)^p \approx u_0^{(2)}(x, y)\ 1/2(z\lambda/d)^2 \qquad (12)$$

if the terms p = 4, 6,.. are small compared to p = 2. This can be shown as follows. Let

$$f_p = 1/p!\ (z\lambda/d)^p\ u_0^{(p)}(x, y).$$

Then equation (12) becomes

$$\sum_{\substack{p=2 \\ (\text{even})}} f_p \approx f_2$$

if

$$|f_p| \lesssim 1/10\ f_2^{\max}.$$

The factor of 1/10 is picked as a figure of merit, but other values may be used. As we shall see, this factor determines the maximum distance that the object can be placed from the second grating G2. Now,

$$|f_2| \le f_2^{\max} = 1/2(z\lambda/d)^2\ u_0^{(2)}{}_{\max}. \qquad (13)$$

By the theorem of Bernstein[10], the derivatives of a bandlimited function are bounded by the maximum value that the function attains. That is,

$$|g^{(p)}(x)| \le (2\pi L)^p\ B_0$$

where $B_0 = (g(x))_{\max}$ and L is the maximum frequency of g(x) in the Fourier domain. Call $2L = \Delta\nu$; we have

$$|f_p| \le 1/p!\ (z\lambda/d)\ (\pi\Delta\nu)^{p-2}\ u_0^{(2)}{}_{\max} = 2/p!\ (z\lambda\pi\Delta\nu/d)^{p-2}\ f_2^{\max}$$

which when compared with equation (13) implies that

$$2/p!\ (z\lambda\pi\Delta\nu/d)^{p-2} \le 1/10,$$

$$z\lambda/d \le (p!/20)^{1/p-2}/(\pi\Delta\nu).$$

The factorial dominates the root process as can be shown using the Stirling's approximation for factorial,

$$(p!/20)^{1/p-2} \approx (\sqrt{2\pi}/20)^{1/p-2}, p/e \text{ for large } p.$$

Therefore the smallest p, (p = 4) is the tightest bound for z, and we have

$$z\lambda/d \lesssim \sqrt{24/20} \;/\; \pi\Delta\nu \approx \delta x/3 \; . \tag{14}$$

Recall that for spatial filtering we require that $\Delta\nu \leq 1/d$. Therefore the most stringent condition is for $\Delta\nu = 1/d$. This is required in order that the shifted object spectrum will not overlap, as shown in Figure 6. Thus the object to G2 distance z in this instance must be less than about 1/6 of a Talbot distance, or more exactly,

$$z \leq 1.1 \; z_T/2\pi. \tag{15}$$

Under the above restrictions as given by either equation (14) of (15) for the maximum distance z, the field in the image plane is given by

$$v(x, y) \approx 1/4(1 - 8/\pi^2) \left\{u_0(x, y) - \frac{1}{(\pi^2/16) - 2} \; (z\lambda/d)^2 \; u_0^{(2)}(x, y)\right\}$$

$$\approx 1/20 \left\{u_0(x, y) + 5/7 \; (z\lambda/d)^2 \; u_0^{(2)}(x, y)\right\}. \tag{16}$$

§3.5 First Order Filtering

The mathematics for this case follows simply from the previous section. Here we filter either the n + m = 1 or n + m = -1 term. The only difference is in the sign of a phase factor which is unimportant when detecting the signal. The field in the image plane becomes for the n + m = +1 case,

$$v(x, y) = C_0 \; C_1 \; e^{2\pi i[x/d + z/z_T]} \left\{u_0(x, y) - u_0(x + z\lambda/d, y)\right\} \tag{17}$$

This surprising result is obtained since the even coefficients are zero. Those terms which contribute under the n + m = 1 condition are $C_m \; C_n + C_m \; C_{m-1}$. This combination implies that for any m, one coefficient will always be even and hence equal to zero. This is very much like ordinary shearing interferometry and we will again show that under a certain condition this is approximately the derivative of the object. We ignore the phase since it is the intensity which is observed in the image plane, and deal with the bracketed terms. The last term is expanded in a Taylor series around $z\lambda/d$ and when combined with $u_0(x, y)$ gives

$$\{\ldots\} = \sum_{p \geq 1}^{\infty} u^{(p)}(x, y) \; (z\lambda/d)^p \; 1/p! \approx u_0^{(1)}(x, y) \; (z\lambda/d).$$

Using the same kind of arguments as in the previous section this approximation is valid if the shift is less than 1/15 δx (equation 18).

$$z\lambda/d \lesssim 1/5\pi\Delta\nu \approx (1/15)\,\delta x. \tag{18}$$

Under the strictest condition $|\Delta\nu| \leq 1/d$ the condition of equation (18) means that the object to G2 distance is

$$z \leq z_T/10\pi. \tag{19}$$

Therefore the field in the image plane for first order filtering under the

conditions of equation (18) or (19), whichever may apply, is given by

$$v(x,y) \approx 1/\pi \; e^{2\pi i[x/d+z/z_T]} \; (z\lambda/d) \; u_0^{(1)}(x, y). \qquad (20)$$

One other case has been under investigation. Here we record the intensity pattern on film or on a diffuser (like a rear-projection screen), then view it with a low pass detector such as the eye. The experimental results were shown in the previous case where no filtering was done. The reader's eye performed the filtering as he observed the results. Unfortunately the mathematics has proven cumbersome. But we hope to find the necessary approximation to yield a simple interpretable solution.

§3.6 Experiments

The Talbot interferometer for testing phase objects was placed on a laboratory optical bench. It used two Ronchi rulings of 10 lines per mm. Although they were quite scratched, they performed satisfactorily because the resultant intensity in the plane of observation is summed over a large number of lines. One grating was mounted for rotational motion while the other had translational movement. These two motions allowed the gratings to be aligned as desired. The gratings were held in bench carriers which accomplished longitudinal motion.

Both He-neon laser and white light sources were used. The laser beam was focused onto a pinhole and thereafter collimated (diameter 50mm). For the white light source experiments, a 500 watt slide projector was used. To increase the throughput an adjustable slit was used instead of a pinhole; it was aligned parallel to the bars of G1. The width of the slit was then made sufficiently narrow so that the self-images would appear with good color contrast. It was discovered that the moiré fringes obtained behind the second grating when both gratings were aligned was a measure of the degree of collimation. This work has been accepted for publication and the manuscript is provided in Appendix B.

The method of observing the interference fringes was to project the image of the object with its fringe structure onto a screen. The phase objects tested were: various lenses, prisms, plastic bags and boxes, the change of index of refraction caused by heat of a candle flame, and drops of plastic resin or varnish arranged into different configurations on glass slides.

Photographs of these experiments were made. Two of these appear in our paper that appeared in Optics Communications, February 1971. A copy of this paper is provided in Appendix A. The photographs are of a candle flame that was placed between gratings separated by about 12 cm. To fully appreciate the filtering aspect of this instrument we have separated the gratings by about 30 cm. with the flame placed close to G1. In this case the multiple-shearing interferences are readily observed by the great number of candle wicks in the field of view. By allowing only the zeroth diffracted order to propagate beyond the spatial filter plane, triple-shearing interferences are obtained, as verified by the presence of the wick which appears at three separate locations corresponding to the amount of shear introduced. Lateral shearing interferences

are obtained when first order filtering is used, as indicated by observing only two wick images. Photographs of this along with some beautiful color pictures for a white light source were shown at the 1971 Annual Spring Meeting of the Optical Society of America that was held in Tucson, Arizona.

§4 The Talbot Autocollimator

We found that collimation of the source was critical when using the Talbot interferometer setup (§3). Otherwise it was not possible to completely darken the field. By increasing the separation of the gratings to its maximum permissible extent, a very sensitive means for accurately locating a point source in the focal plane of the lens was obtained. Thus the problem of accurately and inexpensively collimating the light sources for use with the Fourier Spectrometer was solved. A manuscript on "A Simple Interferometric Method of Beam Collimation" has been accepted for publication in Applied Optics this August. The manuscript is reproduced in Appendix B.

§5 The Talbot Interferometer with Circular Gratings

Earlier (§3), we discussed the use of the Talbot Interferometer for testing optical components. This setup used Ronchi rulings and displayed the derivative of the phase object along a direction transverse to the ruling axis. Thus the testing of an axially symmetric object such as a lens requires that it be rotated for complete examination. Ideally, such objects are well suited for testing with interferometers that give a constant shear to the wavefront in the radial direction. Therefore we intend to modify the Talbot interferometer by replacing the straight line gratings with circular gratings. In this way the radial gradient of the deformed wavefront can be observed. A circular grating (see Fig. 9) is defined in this report as consisting of a number of concentric circular rings of constant radial spacing on a transparent surface. Our description will be brief since the experiments and theory of this new modification are not quite complete. We present here our analysis on whether the circular grating will self-image when illuminated by a plane wave.

§5.1 Theory of the Talbot Effect in Cylindrical Coordinates

The theory for the Talbot set of self-imaging objects in cartesian coordinates has been presented in a paper by W. Montgomery.[11] What Montgomery essentially did was to solve the wave equation while asking the following question: "What are the necessary and sufficient conditions that the object must satisfy in order that a faithful image of it be found in a parallel plane $z = d > 0$?"[12] Our solution uses this approach.

We want to solve the wave equation in cylindrical coordinates for the set of axially symmetric objects of finite aperture which are periodic in the direction of wave propagation, the z-axis of Figure 8. Therefore we have the following boundary conditions:

$$u(r, \varphi, z) = u(r, z) \qquad \text{axial symmetry} \qquad (1)$$

$$u(r, \Delta z) = u(r, 0) \qquad \text{periodicity along z-axis} \qquad (2)$$

$$u(r, 0) = 0 \text{ for } r \geq 1 \qquad \text{finite aperture} \qquad (3)$$

where $u(r, 0)$ is the Talbot set of objects we desire, Δz is the period of the repeating image and the cylindrical coordinates (r, φ, z) are related to the cartesian coordinates (x, y, z) by

$$x^2 + y^2 = r^2; \qquad x = r \cos \varphi; \qquad y = r \sin \varphi.$$

The wave equation in cylindrical coordinates is

$$\frac{\partial^2 u}{\partial r^2} + \frac{1}{r}\frac{\partial u}{\partial r} + \frac{1}{r^2}\frac{\partial^2 u}{\partial \varphi^2} + \frac{\partial^2 u}{\partial z^2} + k^2 u = 0$$

where $u = u(r, \varphi\ z)$, $k = 2\pi/\lambda$, and λ is the wavelength of the light source. Applying the axial symmetry condition equ. (1) to the above equation reduces it to

$$\frac{\partial^2 u}{\partial r^2} + \frac{1}{r}\frac{\partial u}{\partial r} + \frac{\partial^2 u}{\partial z^2} + k^2 u = 0 \qquad (4)$$

Next the separation of variables technique is employed, letting

$$u(r, z) = R(r)\, Z(z) = RZ. \tag{5}$$

The boundary conditions of equ. (2) and (3) become

$$R(1) = 0 \tag{6}$$

$$Z(\Delta z) = Z(0). \tag{7}$$

Inserting equ. (5) into (4) we obtain

$$R''Z + \frac{1}{r} R'Z + RZ'' + k^2RZ = 0.$$

Rearranging this and dividing by RZ we have

$$\frac{R''}{R} + \frac{1}{r}\frac{R'}{R} + k^2 = \text{constant} = -\frac{Z''}{Z} \tag{8}$$

The left and right hand sides of this equation are equal to a constant since they are respectively functions of r and z only. If we let the constant be given by $(k\gamma)^2$ and solve the right hand side of equ. (8), we have

$$Z'' = -k^2\gamma^2 Z$$

which yields the solution

$$Z(z) = Z(0)\, e^{\pm ik\gamma z}.$$

The constant is chosen positive and real ($k^2\gamma^2 > 0$) to avoid evanescent waves that are attenuated within a few wavelengths along the z-axis. These waves would not be present over distances that our instrument will operate. Thus our solution is a wave propagating in a direction given by the direction cosine, γ ($\gamma \leq 1$). Furthermore we choose the positive sign in the exponent since forward propagation is of interest here.

Now the boundary condition of equ. (7) is applied to this solution, giving us

$$e^{ik\gamma\Delta z} = 1 \qquad \text{or} \qquad \gamma_m = \frac{m\lambda}{\Delta z} = m\gamma_1 \leq 1.$$

This last inequality comes from our earlier statement. Hence there is a maximum value that m can obtain,

$$m_{max} = \frac{1}{\gamma_1} - \varepsilon,$$

where $0 < \varepsilon < 1$ is a positive number that makes m_{max} an integer. Thus our eigenvalues, γ_m, form a discrete set due to the self-imaging requirement. Consider now the left hand side of equ. (8) which when multiplied by R yields

$$R'' + \frac{1}{r} R' + k^2(1 - \gamma_m^2)R = 0.$$

Let $\xi = r\, k \sqrt{1 - \gamma_m^2}$ and substitute it into the above equation. We have

$$\frac{d^2R(\xi)}{d\xi^2} + \frac{1}{\xi}\frac{dR(\xi)}{d\xi} + R(\xi) = 0.$$

This is the Bessel's differential equation of order zero that has the solution

$$R(\xi) = J_0(kr \sqrt{1 - \gamma_m^2})$$

Applying the boundary conditions of equ. (6) to this solution gives

$$R(1) = 0 = J_0(\nu_m)$$

where $\nu_m = k\sqrt{1 - \gamma_m^2}$ are the zeros of J_0. Thus our elementary solution is, to within a constant, given by

$$u_m(r, z) = e^{ik\gamma_m z} J_0(\nu_m r).$$

Our total solution is a superposition of all our separate eigenvalue solutions.

$$u(r, z) = \sum_{m=0}^{m_{max}} C_m e^{ikm\gamma_1 z} J_0(kr\sqrt{1 - (m\gamma_1)^2}) \qquad (9)$$

In order to evaluate the C_m's we use

$$\int_0^1 J_0(\nu_m r) J_0(\nu_n r) \, rdr = \frac{1}{2} \delta_{nm} J_1^2(\nu_m) \qquad (10)$$

where ν_m, ν_n are zeros of J_0, and δ_{nm} is the Kronecker delta,

$$\delta_{nm} = \begin{cases} 0, & n \neq m \\ 1, & n = m \end{cases}$$

Our initial condition is $u(r, 0)$, that is $u(r, 0)$ is the Talbot set of objects with axial symmetry. From equ. (9)

$$u(r, 0) = \sum_{m=0}^{m_{max}} C_m J_0(\nu_m r). \qquad (11)$$

By integrating this as follows

$$\int_0^1 u(r, 0) J_0(\nu_n r) \, rdr$$

the C_m's can be determined. Substituting equ. (11) into the above, and exchanging summation and integration yields,

$$\begin{aligned} \int_0^1 u(r, 0) J_0(\nu_n r) \, dr &= \sum_{m=0}^{m_{max}} C_m \int_0^1 J_0(\nu_m r) J_0(\nu_n r) \, rdr \\ &= \sum_{m=0}^{m_{max}} C_m \frac{1}{2} \delta_{nm} J_1^2(\nu_m) \\ &= \frac{1}{2} C_n J_1^2(\nu_n). \end{aligned}$$

Therefore,

$$C_n = \frac{2}{J_1^2(\nu_n)} \int_0^1 u(r, 0) J_0(\nu_n r) \, rdr.$$

Thus our solution for the Talbot set of axial symmetric objects is:

$$u(r, z) = \sum_{m=0}^{m_{max}} C_m e^{ikm\gamma_1} J_0(\nu_m), \quad C_m = \frac{}{J_1 \ \nu_m)} \int_0^1 u(r, 0) J_0(\nu_m r) \, rdr$$

where $m_{max} = \frac{1}{\gamma_1} - \varepsilon$, $\nu_m = k\sqrt{1 - (m\gamma_1)^2}$.

§5.2 Self-Imaging of a Circular Grating

The circular grating (see Fig. 9) can be expressed in a Fourier Series as follows:

$$G(r) = \sum_{m=0}^{\infty} C_m e^{2\pi i m r/a}$$

where $C_m = \alpha \operatorname{sinc} m\alpha$, a is the period and α is that fraction of the period for which the grating is transparent. Our exact solution for the Talbot set of axially symmetric gratings is in Bessel functions which for large arguments behave approximately like a cosinusoidal function.

$$J_0(\nu_n r) \approx \frac{1}{\sqrt{\pi \nu_n r}} \cos(\nu_n r - \tfrac{\pi}{4}); \quad \nu_n r > 25. \tag{12}$$

Therefore our elementary solution in r will build up to a periodic structure like a circular grating if $\nu_m = a/2\pi R$, i.e. $k\sqrt{1 - (m\gamma_1)^2} = a/2\pi R$.

However, the $1/\sqrt{r}$ factor in equ. (12) means that the contrast will diminish with increasing r. That is, an object which belongs to a Talbot set of axially symmetric objects must have decreasing values of transmittance as r increases in order to be faithfully self-imaged. Thus the circular grating only approximately belongs to this Talbot set of objects.

Circular gratings were made on AGFA SCIENTIA 10E75 glass photographic plates. These were used to replace the Ronchi rulings of our Talbot interferometer. The Talbot images observed showed a decreased contrast toward the grating edges which can be explained by the $1/\sqrt{r}$ factor mentioned previously. This may limit the maximum size of the object that can be tested. We have looked at 50 mm diameter objects without difficulty. A full report can not be made at this time as the work is not quite complete.

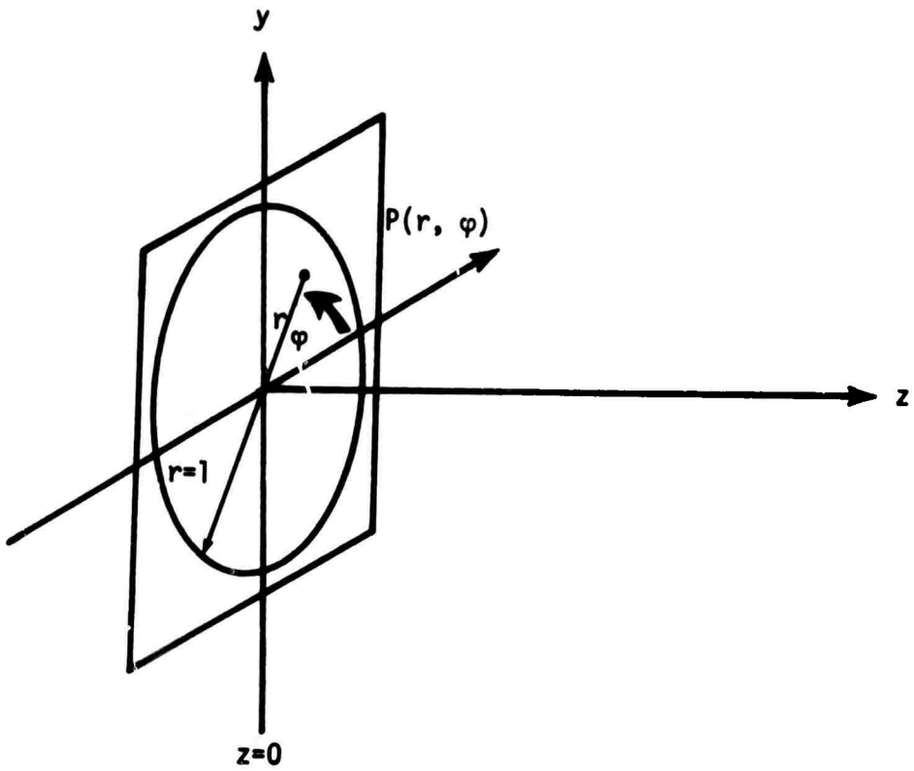

Figure 8. The geometry and coordinates used in §5. Aperture is circular and has values u(r, 0).

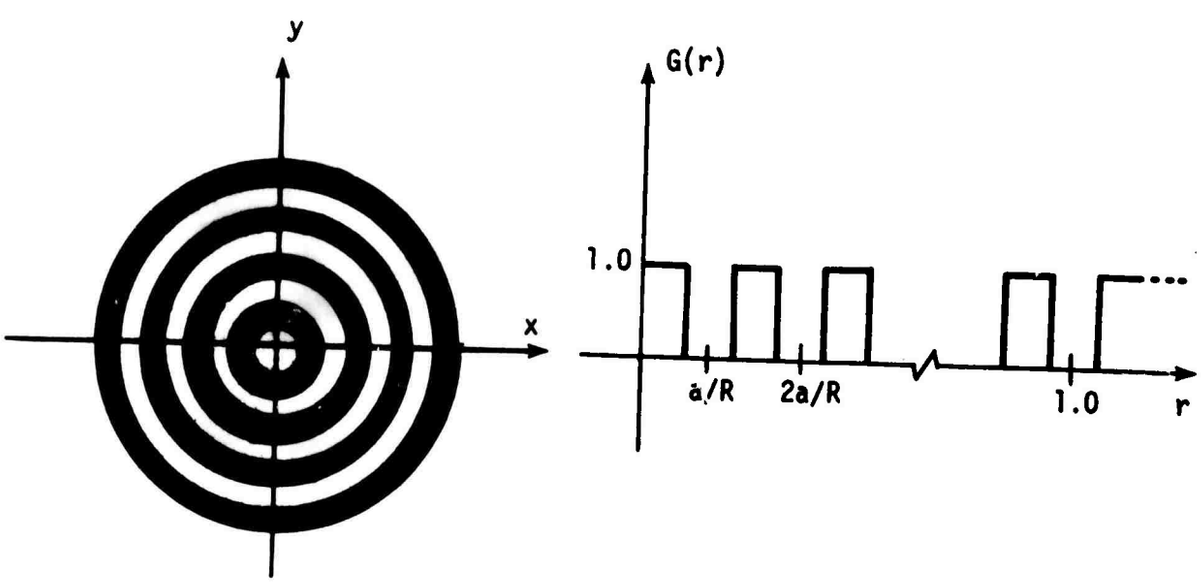

Figure 9. The circular grating. The normalized transmittance function is shown on the right side.

References cited in this report:

1. Talbot F., Phil. Mag., 1836, 9, 401.
   Cowley J. M. and Moodie A. F., Proc. Phys. Soc., 1957, B70, 486.
   Montgomery W. D., J. Opt. Soc. Amer., 1967, 57, 772.
   Winthrop J. T. and Worthington C. R., J. Opt. Soc. Amer., 1965, 55, 373.

2. Ibid.

3. Lohmann A., Proc. Conf. Opt. Instruments and Techniques, 1961, London, Chapman and Hall, 1962, 58.

4. Goodman J., Introduction to Fourier Optics, McGraw-Hill, 1968.

5. Nishijima Y. and Oster G., J. Opt. Soc. Amer., 1964, 54, 1.

6. Lohmann A., loc. cit.

7. Edgar R. F., Optica Acta, 1969, 16, 281.

8. Goodman J., op. cit., 48.

9. Edgar, loc. cit.

10. Arsac J., Fourier Transforms and the Theory of Distributions, Prentice-Hall, 1966, 315.

11. Montgomery W.D., loc. cit.

12. Ibid.

List of all participating scientists:

Adolf W. Lohmann, principal investigator, Professor of Applied Physics
Donald E. Silva, research assistant

Aside from this contract (AF F 19628-69-C-0268), the principal investigator has been awarded the following grants:

California Division of the American Cancer Society "Optical Processing of X-ray Planigraphs",	$6,120	SP-530 9/1/70-8/31-71
National Science Foundation "Holographic Information Processing"	NSF GK-28563X $38,000	5/1/71-4/30/72

Publications:

"An Interferometer Based on the Talbot Effect", Opt. Comm. 2:413-415.
"A Simple Interferometric Method of Beam Collimation", submitted to Appl. Opt.

BLANK PAGE

AN INTERFEROMETER BASED ON THE TALBOT EFFECT

A. W. LOHMANN and D. E. SILVA
Department of Applied Physics and Information Science,
University of California, San Diego, La Jolla, California 92037, *USA*

Received 28 December 1970

The moiré effect is very sensitive in detecting small differences between two similar gratings. These differences might be caused by an object with phase gradient placed between the two gratings. The performance of such an instrument can be understood in terms of the "Talbot effect" (also called "Fourier imaging" or "self-imaging"). Slight modifications provide shearing interferences and the second derivative of the object.

The moiré effect reveals very small imperfections of two gratings placed on top of each other. Lord Rayleigh used this effect for testing diffraction gratings. The same basic idea has been used for many other purposes. For example, in electron microscopy the imperfections in two pieces of crystal lattice can be made visible in this way [1]. Essentially the same moiré effect is utilized for studying the shape of a diffusely reflecting surface, when the shadow of a grating falls onto that surface. The grating shadow is observed through the same grating [2]. Also the shape of a refracting object can be investigated by means of the moiré effect [3]. The refracting object is placed before or behind a first grating (fig. 1). The shadow of the first grating will be deformed due to the refractive gradient. The moiré fringes observed behind the second grating placed at a distance z from the object are lines of equal deviation [eq. (1)].

$$\epsilon_x(x, y) = md/z; \qquad m = 0, \pm 1, \pm 2 \ldots \quad (1)$$

We intend to extend this method of observing refractive gradients by means of moiré. As described so far this method is based entirely on rays. This point of view is not satisfactory since it is known that wave optical color effects occur when white light passes through two gratings at a finite distance. This happens with uncollimated [4] and with collimated light [5]. Such color effects may well prove to be useful. A more important objection against the ray-optical point of view is the inability to explain the fundamental limitation of this method. Based on eq. (1), one might suspect that an arbitrarily small deflection angle can be detected if only the distance z of the two gratings is sufficiently large. Since such unlimited detectibility is never attainable

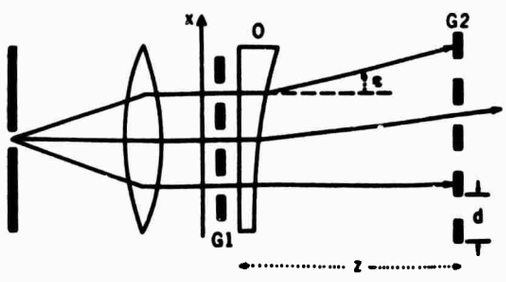

Fig. 1. The Talbot interferometer. G1, G2 gratings with period d; ray deflection angle ϵ in object O.

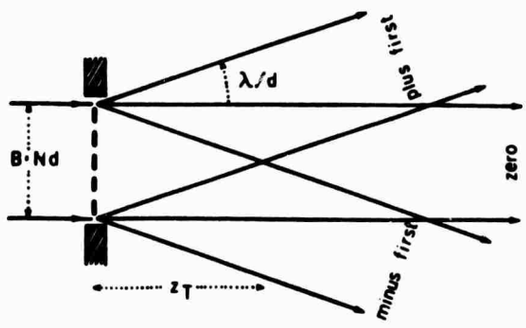

Fig. 2. Overlapping diffraction orders behind a grating of finite width $B = Nd$.

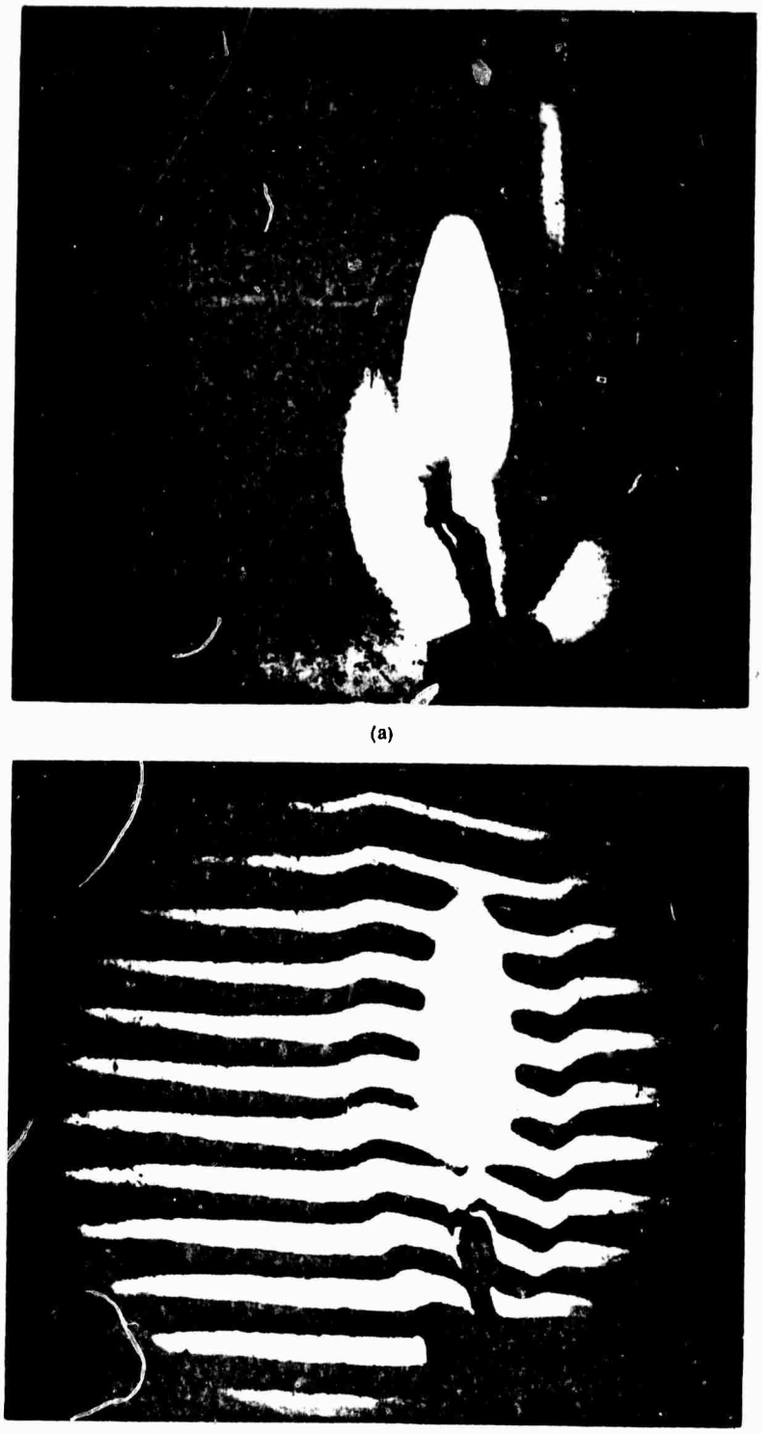

(a)

(b)

Fig. 3. Talbot interferences with a candle flame as object between the two gratings. a. Gratings parallel. b. One grating slightly rotated.

one might try to patch on the following wave-optical argument.

The light passing through a grating slit of width $d/2$ does not behave like a ray anymore after it has travelled over a distance z_R where the diffraction spread $z_R\lambda/(d/2)$ equals the slit width $d/2$ [eq. (2)].

$$z_R\lambda/(d/2) = d/2 \; ; \quad z_R = d^2/4\lambda \; . \tag{2}$$

Based on this criterion one might expect ϵ_R to be the smallest detectable deflection [eq. (3)].

$$\epsilon_R = d/2z_R = 2\lambda/d \; . \tag{3}$$

With $\lambda = 0.5 \times 10^{-3}$ mm and $d = 10^{-1}$ this leads to $\epsilon_R = 10^{-2}$, which is only moderately good.

Fortunately the method is capable of detecting angles much smaller than ϵ_R [eq. (3)]. This is due to the Talbot effect [6], which is also known as "Fourier imaging" [7] and "self-imaging" [8]. Talbot discovered about 135 years ago that images can be formed without any lenses or mirrors if the object is a grating which is illuminated in collimated monochromatic light. These "Talbot images" occur at distances $2d^2/\lambda$, $4d^2/\lambda$, etc. behind the grating. When a second grating at a slight angular rotation to G1 is placed into the plane of a Talbot image, moiré fringes of high contrast are observed. These moiré fringes will be deformed if a refractive phase object is placed for example close to the first grating. As before these moiré fringes indicate lines of equal deflection by the object [eq. (1)].

The largest possible distance z_T (or maybe $2z_T$) depends on the finite width $B = Nd$ of the first grating. At z_T the first grating diffraction orders have moved to both sides by half of the grating width B [fig. 2; eq. (4)].

$$z_T\lambda/d = B/2 = Nd/2 \; ; \quad z_T = Nd^2/2\lambda \; . \tag{4}$$

When the two gratings are separated by z_T the smallest detectable deflection ϵ_T is now smaller by a factor $2N$, where N is the number of periods in the first grating [eq. (5)].

$$\epsilon_T = d/2z_T = \lambda/Nd = \lambda/B = \epsilon_R/2N \; . \tag{5}$$

We have performed some experiments with this "Talbot interferometer" as shown in fig. 1. In fig. 3a the object is a flame, and again in fig. 3b, but now with the second grating slightly rotated around the optical axis. In some additional experiments we have placed a telecentric lens system behind the Talbot interferometer. When introducing a spatial filter into this telecentric system and rejecting everything but the zeroth diffraction order from the two-grating system one observes in essence the second derivative $\partial^2 u/\partial x^2$ of the object $u(x,y)$. When shifting the spatial filter to one of the first grating diffraction orders the image represents shearing interferences $u(x + \lambda z/d, y) - u(x, y)$. In a white light one obtains beautiful color fringes which are unlike ordinary interference fringes. For example for a specific grating distance the image contains many blue-orange fringes. These color fringes are of such high contrast that E. Lau found a similar setup useful in designing tablecloths [9]. Our method is also applicable for the detection of small differences between two quite irregular but similar objects. One begins by recording photographically the fringes from the first object. After development the photograph is placed where the fringes had been observed. The first object is now replaced by the second object, which might actually be the first object but somewhat deformed. The moiré fringes between subsequently produced Talbot interference fringes will reveal small differences between the two objects. The quantitative evaluation is similar to that for Lau's dupligram method [10] and for life-fringe holographic interferometry.

REFERENCES

[1] J. W. Menter, Advan. Phys. 7 (1958) 299.
[2] H. Takasaki, Appl. Opt. 9 (1970) 1467.
[3] Y. Nishijima and G. Oster, J. Opt. Soc. Am. 54 (1964) 1.
[4] E. Lau, Ann. Physik (6), 2 (1948) 417.
[5] A. Lohmann, Proc. ICO Conf. Opt. Instr., ed. K. J. Habbell (London, 1961) p. 58.
[6] F. Talbot, Phil. Mag. 9 (1836) 401.
[7] J. M. Cowley and A. F. Moodie, Proc. Phys. Soc. (London) B70 (1957) 486, 497, 505; B76 (1960) 378.
[8] W. D. Montgomery, J. Opt. Soc. Am. 58 (1968) 1112.
[9] E. Lau, Wiss. Ann. 1 (1952) 43.
[10] E. Lau, Optik 12 (1955) 23.

Appendix B

A SIMPLE INTERFEROMETRIC METHOD OF BEAM COLLIMATION

by

Donald E. Silva

Department of Applied Physics and Information Science

University of California, San Diego

La Jolla, California 92037

April 1, 1971

There are two common methods of determining the degree of collimation: autocollimation and shearing interferometry. The simplest method is the autocollimation technique, but it only indicates collimation by comparing the size of the source with its image. On the other hand the spacing of the fringes in shearing interferometry is a direct measure of the degree of collimation.[1] Recently, Langenbeck derived a method that used two tiny corner-cube reflectors to sample the beam. In this fashion he was able to translate the measurement from fringe spacing to fringe rotation, resulting in increased sensitivity.[2] The method presented here is an application of the Talbot interferometer[3] and has the same limitations as the other interferometric techniques. The main advantages of this technique are the inexpensive components (two Ronchi rulings) and the relative insensitivity to component alignment.

As Talbot observed in 1837, an image of a grating appears at integral multiples of the distance $2d^2/\lambda$ (where d is the grating period) when the grating is illuminated by a plane monochromatic wave. A Ronchi ruling would therefore be imaged at $2d^2/\lambda$, $4d^2/\lambda$, etc. If we place another identical Ronchi ruling in one of these self-image planes (see Figure 1) moiré fringes will be formed, as observed by J. Burch.[4] The fringe spacing P can be calculated by using the vector diagrams described by Rogers[5] to be

$$P = d/2 \sin(\theta/2) \qquad (1)$$

where θ is the angle with which the two gratings meet. As the grating G2 is rotated around the optical axis, the fringe spacing increases until we have uniform brightness (or darkness) when grating bars of G1 and G2 are parallel to each other.

The plane wave that illuminates G1 of the interferometer is obtained by placing a point source at the focus of a lens as shown in Figure 1. When this lens is defocused the plane monochromatic wave becomes spherical. Cowley and

Moodie[6] have shown that the positions of the self-image planes of a grating illuminated by a spherical wave are given by

$$1/Z_J + 1/Z_W = 1/2JZ_T, \tag{2}$$

where J is a positive integer, $1/Z_W$ is the curvature of the incident wave at G1, Z_J is the location of the self-image as measured from G1 and Z_T is the distance $2d^2/\lambda$. The self-image will be magnified by a factor

$$M = 1 + Z_J/Z_W . \tag{3}$$

This image, when superimposed with the second grating, again produces moiré fringes. Now the grating G2 is rotated around the optical axis until the grating bars of G1 and G2 are parallel to each other. In this case, the Rogers vector diagram gives a fringe spacing

$$P = d_1 d_2/|d_1 - d_2|$$

where d_1 is the period of the self-image, d_2 the period of the second grating, and $d_1 = Md$. The fringe spacing in terms of the grating period d is therefore

$$P = Md/|M - 1|.$$

Thus the fringe spacing is a quantitative measure of the degree of collimation since $|M - 1|$ is proportional to the curvature $1/Z_W$.

Now we want to discuss the accuracy obtainable, that is, the smallest detectable deviation from perfect collimation. If the collimation is perfect, the magnification M of the Talbot image is 1, and hence the moiré period P is infinite. Thus our task is to find how small must the period P become in order to be detectable. Experience has shown that the presence of a moiré effect is clearly visible if at least one half of the moiré period P falls

within the limited field of observation with width B. Thus one fringe will be detected whenever the number of lines between grating G2 and the image of G1 differ by one-half. With divergent illumination we count N lines of G2 in the observation field of width B and N - 1/2 lines of the image of G1. Thus the magnification M required for fringe detection is bounded by

$$M \geq \frac{N}{N - 1/2} \approx 1 + 1/2N, \tag{4}$$

and in convergent illumination,

$$M \leq \frac{N}{N + 1/2} \approx 1 - 1/2N. \tag{5}$$

By combining equations (2) and (3) we have

$$M = (1 - 2J\ Z_T/Z_W)^{-1} \approx 1 + 2J\ Z_T/Z_W. \tag{6}$$

If M falls outside the bounds of equ. (4) and (5), no fringes will appear, limiting the sensitivity of this test. Solving equ.(6) with the bounds of equ. (4) and (5) we find that the minimum detectable field curvature $1/Z_W$ is

$$|1/Z_W| \geq (4NJ\ Z_T)^{-1}$$

where the absolute signs obviate the necessity of assigning a sign convention for field curvature. By substituting equ. (2) into the above equation we obtain, for $N >> 1$,

$$|1/Z_W| \gtrsim (2N\ Z_J)^{-1} \tag{7}$$

From equ. (7) it follows that a large value of Z_J is desired in order to detect small collimation defects $1/Z_W$. The furthest distance to which we can go is limited by the "walkoff" of the first-order grating diffraction. As indicated in Figure 2, the longest distance at which there is still a connected interference field of width D is at $Z_J = Dd/2\lambda$. Perhaps one could perform collimation tests up to about twice this distance, but we will restrict ourselves

to $Z_J \leq Dd/2\lambda$. Inserting this limit into equ. (7), together with $N = D/d$, we get

$$|1/Z_W| \geq 2\lambda/D^2. \tag{8}$$

The curvature of the wave incident on G1 is related to the defocusing of the collimating objective by

$$\left|\frac{1}{Z_W}\right| = \frac{|f - Z_0|}{Z_G|f - Z_0| + Z_0 f} \approx \frac{|f - Z_0|}{Z_0 f} \tag{9}$$

where Z_0 is the distance of the collimating objective from the point source, Z_G is the distance from objective to G1, and f is focal length of the objective lens. The approximation is permissible since the distance $Z_G << Z_0 f/|f - Z_0|$ in the test. Call $\delta = |f - Z_0|$ the focusing error, and substitute equ. (8) into equ. (9). We have

$$\delta \geq 2\lambda(f/D)^2 \tag{10}$$

where we have used the fact $Z_0 \approx f$. Thus the focusing error is simply related to the wavelength, and the square of the focal length to beam diameter ratio.

The focusing error can be reduced by simply rotating one grating with respect to the other, thereby producing moiré fringes in the field of observation. In this fashion we change our detection scheme from the condition of uniform brightness to a system of rotating fringes. It is known that fringe detection is more accurate than use of the uniform brightness condition. We rotate both gratings in opposite directions by angles $\theta/2$ with the y-axis. If both gratings have the same period, moiré fringes will appear in the field of observation parallel to the x-axis with spacings given by equ. (1). When the periods are unequal, the fringe spacing is given by

$$P = \frac{d_1 d_2}{(d_1^2 + d_2^2 - 2d_1 d_2 \cos\theta)^{1/2}} \approx \frac{d_1 d_2}{|d_1 - d_2|}$$

where the approximation is for small angular rotations of θ, and d_1, d_2 are the grating periods of G1 image and G2 respectively. It can be shown by using the vector arguments of Rogers that these fringes of unequal grating periods are rotated through an angle ϕ with respect to the x-axis, and the direction of this rotation depends on whether the illumination is converging or diverging. Thus the experimenter knows in which direction to move the objective lens. This rotation is related to the magnification M by

$$M = \frac{\cot\theta/2 + \tan\phi}{\cot\theta/2 - \tan\phi} .$$

Substituting this equation into equ. (3) we obtain

$$\frac{1}{Z_W} = \frac{1}{Z_J} \frac{2\tan\phi}{\cot\theta/2 - \tan\phi} \qquad (11)$$

Our ability to measure ϕ limits the sensitivity of this test. If we say the minimum detectable fringe angle ϕ is about one-half of a fringe (see Figure 3), then equation (11) reduces to

$$|1/Z_W| \geq 2\lambda/D^2.$$

This lower bound is identical to that of the uniform brightness condition, equ. (8). In the laboratory one-quarter of a fringe was easily discernible, producing results which were a factor of two better than predicted. If we want to achieve even higher accuracy we may use photodetectors instead of the eye. Assuming 1% brightness accuracy, we can detect fringes one hundred times larger than the field of view. Hence the photoelectrical approach would improve the detectibility of collimation errors by a factor of about fifty over that which was predicted.

The visual experiments have confirmed our theoretical performance predictions. An objective lens of 20 cm focal length was used to produce a 5 cm beam. The light from a helium-neon laser was focused with a 3.9 mm focal

length lens onto a 6 μ pinhole. The position accuracy was 0.001 cm, whereas the calculated accuracy was 0.002 cm. This improvement was due to the fact that 1/4 fringe was used with the angular measurement technique.

Last, one can improve the accuracy of the test by increasing the distance Z_J. This distance was limited by the walkoff as shown in Figure 2. By the addition of one or two mirrors placed where the borderline rays of the zeroth diffraction order propagate (Figure 2), the diffracted first-order beam can be reflected back into the zeroth-order beam to create the shearing interferences. This should increase Z_J and the accuracy of the test manyfold. However, this has not been verified experimentally.

The author is indebted to Adolf Lohmann for his support and interest in this work and for his helpful suggestions in the preparation of this letter. This work was performed under Air Force contract AF-F19628-69-C-0268.

REFERENCES

1. Murty, M. V. R. K., Appl. Opt. 3, 531 (1964)

2. Langenbeck, P., Appl. Opt. 9, 2590 (1970)

3. Lohmann, A. W., Proc. Conf. Opt. Instruments and Techniques (1961) London, Chapman and Hall (1962), 58

   Klages, H., J. Phys. 28, C2-40 (1967).

   Lohmann, A. W., and Silva, D. E., Opt. Comm. 2, 413 (1971).

4. Burch, J., Progr. Opt. 2, 75 (1963)

5. Rogers, G. L., Proc. Phys. Society (London) 73, 142 (1959)

6. Cowley, J. M. and Moodie, A. F., Proc. Phys. Society B70, 486 (1957)

FIGURE CAPTIONS

1. Talbot Interferometer setup for observing fringes due to defocusing of collimator objective ($Z_0 \neq f$). Fringes are observed on G2.

2. The self-imaging effect occurs within overlapping orders. Test done at distance where the two first order diffraction spots begin to separate.

3. Moiré fringes which are rotated through angle ϕ because of defocusing of collimator objective.

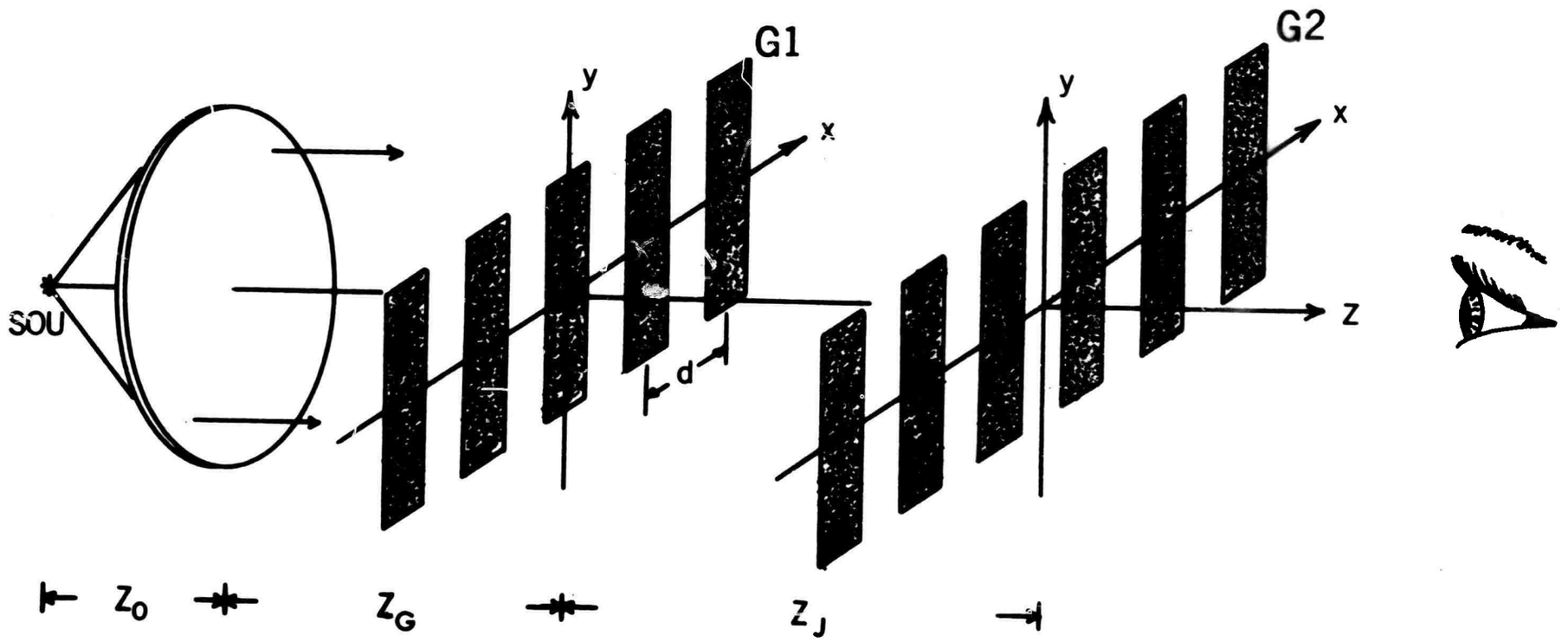
G1
G2
y
x
y
x
z
SOU
d
Z_0
Z_G
Z_J

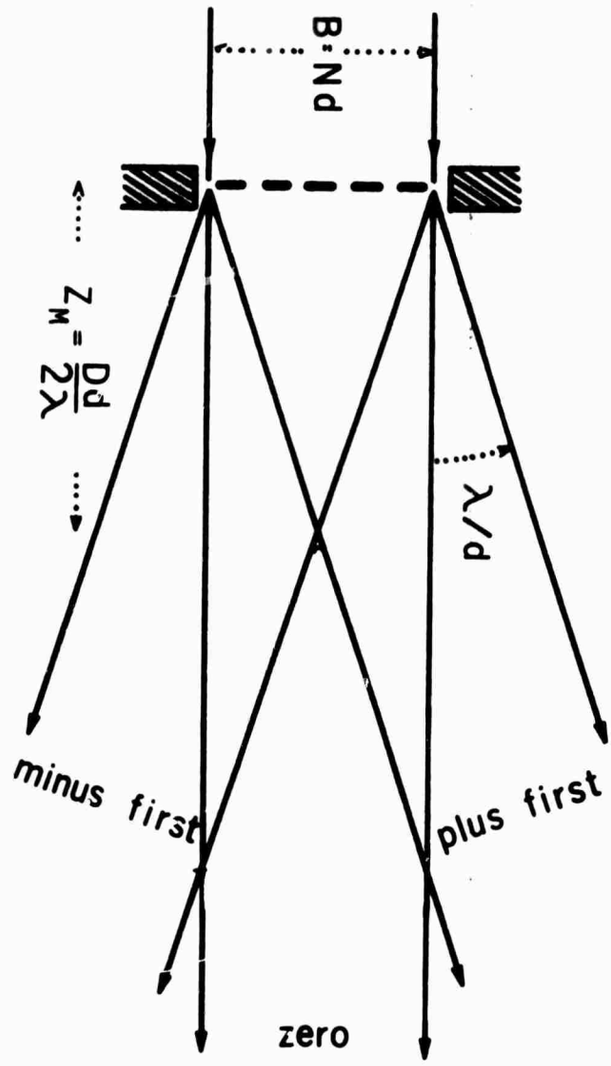
B=Nd
$Z_M = \frac{Dd}{2\lambda}$
λ/d
minus first
plus first
zero

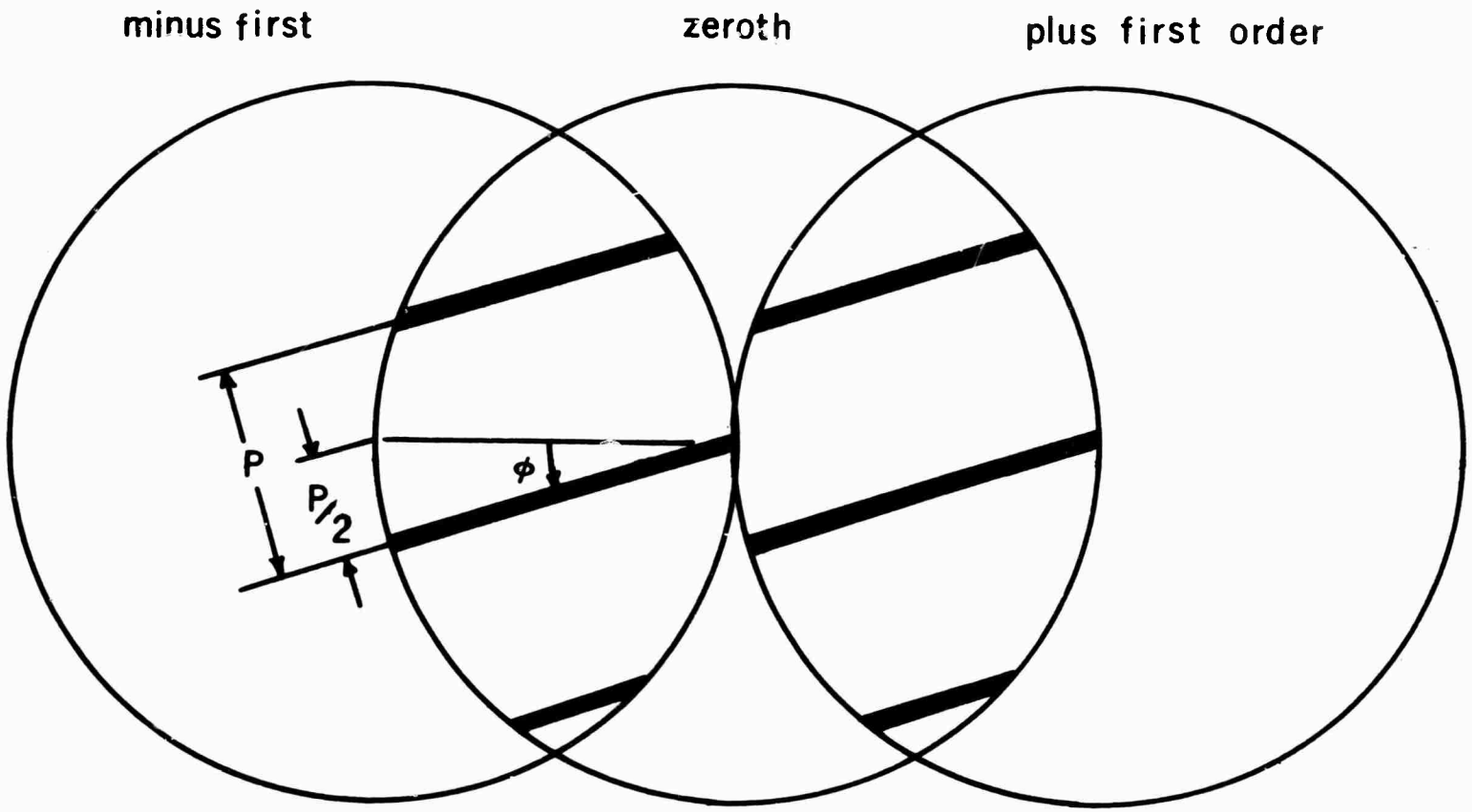
minus first
zeroth
plus first order
P
P/2
φ